JGR Space Physics

RESEARCH ARTICLE
10.1029/2026JA035082

Analysis of Chorus Wave Power on Burst-Mode Timescales During the Van Allen Probes Era

R. Black[1,2], O. Allanson[1,3], N. P. Meredith[2], A. Hillier[4], and D. P. Hartley[5]

[1]Department of Earth and Environmental Sciences, Centre for Environmental Mathematics, University of Exeter, Penryn, UK, [2]British Antarctic Survey, Natural Environment Research Council, Cambridge, UK, [3]Space Environment and Radio Engineering, Electronic, Electrical and Systems Engineering, School of Engineering, University of Birmingham, Birmingham, UK, [4]Department of Mathematics, University of Exeter, Exeter, UK, [5]Department of Physics and Astronomy, University of Iowa, Iowa City, IA, USA

Abstract Interactions between whistler-mode chorus waves and electrons are a key driver of dynamics in Earth's radiation belts. These global dynamics are often described using Fokker-Planck diffusion models. Whilst, in many cases, such models effectively describe the large scale changes within the region, they often rely upon spatially and temporally averaged representations of the wave properties. However, observations have shown that whistler-mode chorus can display large sub-second powers that challenge model assumptions and potentially give rise to non-diffusive processes. Here, we investigate the power of whistler-mode chorus on sub-second timescales using the high-resolution data capture mode on the Van Allen Probes' Electric and Magnetic Field Instrument Suite and Integrated Science (EMFISIS). We show that peak chorus power on sub-second timescales is regularly larger than the corresponding spacecraft "survey" power by over a factor of 100. The work also explores the magnetospheric conditions under which the largest sub-second power variability of chorus waves is observed, and we find that trends vary across different chorus frequency bands. Notably, the largest powers are observed in the lower-band frequency range during active conditions and between 21:00–12:00 MLT, where >46% of burst samples contain an instantaneous wave intensity that exceeds $2.25 \times 10^4\ pT^2$. Further, binning the lower-band power by the ratio of plasma-to-gyrofrequency separates the waves into two distinct low and high variability populations. The results quantify sub-second wave power variability that may influence energetic electron dynamics not currently captured in time-averaged wave models.

Plain Language Summary Whistler-mode chorus is an electromagnetic emission excited in Earth's magnetosphere that can interact with electrons in the outer radiation belt. Through such interactions, electrons can be accelerated, or scattered into the atmosphere. Over long timescales, the resulting global changes in the electron population are typically modeled as a diffusive process. The wave power spectrum is a key input to these models. However, spacecraft measurements show that chorus wave power can be intense and highly variable on short timescales. These features may not be captured in traditional wave statistics due to a variety of spatial and temporal averaging. Such intense and rapidly varying waves may also violate assumptions required for the diffusive framework, and can instead result in interactions with distinct particle responses. Using high-resolution spacecraft data, we show that maximum chorus wave powers on short timescales can be orders of magnitude larger than those inferred from averaged spacecraft surveys. Under certain magnetospheric conditions, we also identify a population of waves for which up to half may violate assumptions in current radiation belt modeling. Our study motivates further work to investigate how the short-timescale variability of chorus wave power could affect modeling of wave-particle interactions.

Key Points:

- Sub-second chorus wave power in different frequency bands are investigated using the EMFISIS burst- and survey-mode data
- Lower-band power was largest during active times (AE > 300 nT) whilst power variability peaked at low f_{pe}/f_{ce} (<5) across all activities
- Large ratios of maximum burst-to-survey power were observed in lower-band at low f_{pe}/f_{ce} (<5), and upper-band over all conditions

Supporting Information:

Supporting Information may be found in the online version of this article.

Correspondence to:

R. Black,
rb894@exeter.ac.uk

Citation:

Black, R., Allanson, O., Meredith, N. P., Hillier, A., & Hartley, D. P. (2026). Analysis of chorus wave power on burst-mode timescales during the Van Allen Probes era. *Journal of Geophysical Research: Space Physics*, *131*, e2026JA035082. https://doi.org/10.1029/2026JA035082

Received 13 JAN 2026
Accepted 5 MAY 2026

Author Contributions:

Conceptualization: R. Black, O. Allanson, N. P. Meredith
Data curation: R. Black
Formal analysis: R. Black, O. Allanson, N. P. Meredith, A. Hillier, D. P. Hartley
Funding acquisition: O. Allanson, N. P. Meredith, A. Hillier
Investigation: R. Black, O. Allanson, N. P. Meredith, A. Hillier, D. P. Hartley
Methodology: R. Black, O. Allanson, N. P. Meredith, A. Hillier, D. P. Hartley
Project administration: O. Allanson, N. P. Meredith, A. Hillier
Resources: R. Black, O. Allanson, N. P. Meredith, A. Hillier
Software: R. Black

1. Introduction

Chorus waves are electromagnetic emissions in the whistler-mode that can be found within Earth's magnetosphere, primarily outside of the plasmasphere (Burtis & Helliwell, 1969). These waves exist at frequencies between the lower-hybrid frequency, f_{LHR}, and the minimum of the electron gyro frequency, f_{ce}, or the plasma frequency, f_{pe}. Their power spectrum often exhibits a lower- and upper-band within this range, separated by a power gap at $0.5f_{ce}$ (Tsurutani & Smith, 1974). Crucially, chorus waves have been identified as one of the primary drivers of variability in the flux of electrons within Earth's outer radiation belt; a population of high energy electrons that form a toroidal-shaped region around the Earth. The radiation belt electrons, which span across the

Supervision: O. Allanson, N. P. Meredith, A. Hillier
Validation: R. Black, O. Allanson, N. P. Meredith
Visualization: R. Black, O. Allanson, N. P. Meredith, D. P. Hartley
Writing – original draft: R. Black, O. Allanson, N. P. Meredith, A. Hillier
Writing – review & editing: R. Black, O. Allanson, N. P. Meredith, A. Hillier, D. P. Hartley

sub-relativistic to relativistic/ultra-relativistic energy range, can undergo resonant interactions with chorus waves that lead to both acceleration (e.g., Horne et al., 2005), and pitch angle scattering into the atmosphere (e.g., Ni et al., 2008). The radiation belt electron populations often spatially overlap with the orbits of satellites, where relativistic and ultra-relativistic electrons can damage instrument electronics through deep-dielectric charging (Lohmeyer et al., 2015). Given the reliance of modern society on satellites, it is important to accurately describe the wave fields to improve predictions of the radiation belt electron population variability.

The long-term changes (over $\sim$ hours to days) in radiation belt phase space density are often described using quasilinear diffusion simulations (e.g., Albert et al., 2009; Drozdov et al., 2015; Fok et al., 2008; Glauert et al., 2014; Reeves et al., 2012; Subbotin et al., 2010; Varotsou et al., 2005; Varotsou et al., 2008). In this formalism, it is assumed that waves are small perturbations to the background quasi-dipolar field controlling the particle motion. This means that many, successive wave-particle interactions, which take place on the $\sim ms$ timescale associated with a few wave periods, will follow a "random-walk" in phase space. This "random-walk" is described in quasilinear diffusion models by calculating pitch angle and energy diffusion coefficients (Kennel & Engelmann, 1966) that depend upon the background field, wave properties, and plasma conditions. Resulting simulations have been shown to accurately reproduce the cumulative effects of pitch angle scattering (Lyons et al., 1972) and acceleration (Summers et al., 1998) that takes place over many particle drift periods. To calculate these coefficients, models of the wave intensity and wave normal angle are required. These models are often parameterized spatially, as well as by some activity index, such as AE, Kp or Dst, by using spacecraft observations (Aryan et al., 2020, 2021; Agapitov et al., 2015; Meredith et al., 2020; Wang et al., 2019).

There are a number of convenient simplifications, however, that are often taken when developing these models. As it stands, most statistical surveys of spacecraft data use wave intensity averages in their respective spatial and temporal binning. These wave averages are calculated on timescales that are much larger than that of a wave-particle interaction, consistent with the timescales upon which phase space density evolves within the quasi-linear diffusion framework (Aryan et al., 2021; Meredith et al., 2020; Wang et al., 2019).

Additionally, most, but not all models (where Artemyev et al. (2022) is an example of an exception) make use of the "survey" data collection mode of satellites. In this mode, the raw waveform data is processed on-board due to limitations on the data volume for the instrument telemetry and is thus provided at a lower temporal resolution than that which may be achieved from the burst-mode data.

Finally, whilst there have been examples of numerical implementation of spectra into wave models (e.g., Wong et al., 2024), often the wave spectra is simplified for computational ease. This simplification is usually performed by assuming that wave power distributions with respect to frequency for both lower-band and upper-band chorus are a Gaussian around their respective central frequency (Glauert & Horne, 2005; Lyons, 1974; Shprits et al., 2008). This is compatible with the conditions of quasilinear theory, namely that the waves are broadband with sufficient frequency bandwidths (e.g., Karpman, 1974), and statistical analysis of whistler-mode waves in the solar wind have suggested that this criterion is mostly fulfilled in 8 s wave measurements (Tong et al., 2019). However, key features of the chorus wave spectra could be missing, even in the quasilinear regime. The frequency attributed to a given wave defines the resonant energy of a particle with which it would interact (e.g., Kennel & Petschek, 1966). To this point, test particle simulations have demonstrated the importance of correctly specifying the frequency spectrum (Allanson et al., 2024) in determining particle behavior.

Whilst all of the above simplifications are useful for incisively incorporating wave effects into quasilinear diffusion models, it is important to recognize that there are a number of limitations. High resolution wave observations (Agapitov et al., 2014; Cully et al., 2008; Cattell et al., 2008; Kellogg et al., 2010; Li, Bortnik, et al., 2011), taken on a sampling frequency of either 16 or 32 kHz, have revealed the existence of high-intensity waves with significant spectral structure such as rising and falling frequency tones, and small frequency bandwidths. In this work, we will focus on two particular implications introduced by such high-intensity waves; first, upon trends seen in wave distributions, and second, upon approximations required by quasilinear diffusion theory.

Considering the former, Tyler et al. (2019a, 2019b) used the higher-resolution 'burst' mode of the EFW instrument on Van Allen Probes B (Wygant et al., 2013), which has a sampling frequency of 16 kHz, to investigate peak whistler-mode wave amplitudes averaged over 0.125 s. It was shown that whistler-mode peak amplitudes have different spatial distributions and activity-dependent trends to that of averaged intensity commonly used in

statistical models. This suggests that drawing conclusions on global wave behavior from averaged statistics alone may not be capturing the full picture.

Considering the latter, high-intensity, coherent chorus waves may additionally break assumptions required by the quasilinear diffusion theory. In order to have longtime, diffusive behavior of particles in velocity space, subsequent wave-particle interactions must be stochastic, similar to a random walk. There are two implications of this that motivate the work presented in this paper. First, the derivation of quasilinear theory in the limit of resonant diffusion (wave growth rates tend to zero) requires wave spectra to be statistically stationary (quasi-static) over the diffusion timescale (Kennel & Engelmann, 1966). Therefore, if there are rapid changes in the wave spectra on the subsecond timescale, indicative of, for example, rising or falling tones, this assumption may not be satisfied by the waves.

Second, to have uncorrelated wave-particle interactions, we must have random wave-gyroangle phases, ensuring that each successive resonance experienced by a particle is independent, and not determined by the previous (see discussion in e.g., Artemyev et al., 2025; Karpman, 1974, and references therein). This is known as the "random phase approximation". From this comes the requirement that waves must have small wave amplitudes with respect to the background field, or equivalently, large frequency bandwidths (e.g., see Equation 1 in Allanson et al., 2024). If we have comparatively high wave amplitudes, or small bandwidths, particle responses can instead become nonlinear and deterministic (e.g., Bortnik et al., 2008). Such nonlinear interactions can lead to more rapid acceleration than is predicted by quasilinear theory (e.g., Foster et al., 2017; Kurita et al., 2018). However, the true effect of such interactions is difficult to diagnose because observed wave properties (jumps in wave phase and frequency variations) can also reduce the efficiency of nonlinear interactions (Zhang et al., 2020), especially when considering timescales longer than a bounce period (Tao et al., 2025). Relating this once more to spacecraft measurements, it is important to understand when, where and how often we may observe high-amplitude waves, and to what extent they are being smoothed out in wave "surveys".

In summary, looking at the temporal variability of chorus wave power on high-resolutions alongside the averaged, commonly used survey data could help to evaluate their impact on a more global scale, and for use in radiation belt modeling. Regarding this point, our analysis examines the conditions under which the survey-mode data is representative of underlying waveforms observed in the high-resolution burst-mode data. We answer this question by breaking it down into three parts. First, how do the global distributions of peak chorus power and underlying 6 s variability compare to survey distributions? Second, how can we characterize the differences in these statistics for low frequency chorus emissions, lower-band and upper-band chorus emissions? Finally, what are the conditions associated with high, or low, power variability in the chorus populations?

There are two types of magnetic field power spectral density (PSD) analyzed within this study; first, PSDs that are created by the on-board survey-mode processing of waveforms, and, second, PSDs created at higher resolutions, on a sub-6 s timescale, using raw waveforms measured by burst-mode on the EMFISIS instrument. In Section 2, we present the techniques used to create both of these PSD types. We additionally describe how chorus waves were identified within the data set, and how the power in common chorus wave frequency ranges, namely low frequency, lower-band and upper-band chorus, is calculated. Distributions of peak magnetic field power and power variability of chorus on sub-6s timescales are presented in Section 3. The distinctions and similarities between chorus frequency ranges, and potential implications for wave model averaging, are discussed in Section 4, and our conclusions are presented in Section 5.

2. Van Allen Probes Observations

This study utilizes measurements from the Van Allen Probes satellite mission (Mauk et al., 2013) from 7 November 2012 until 14 October 2019. The twin satellites (*A* and *B*) orbited in and out of the heart of the radiation belts up to three times a day, taking measurements of electromagnetic fields, waves and eV-GeV particles. Below we will describe the "survey-mode" and "burst-mode" wave measurements from the EMFISIS instrument (Kletzing et al., 2013, 2023) aboard these satellites, all other parameters required for our analysis, and how chorus events were selected from the observations.

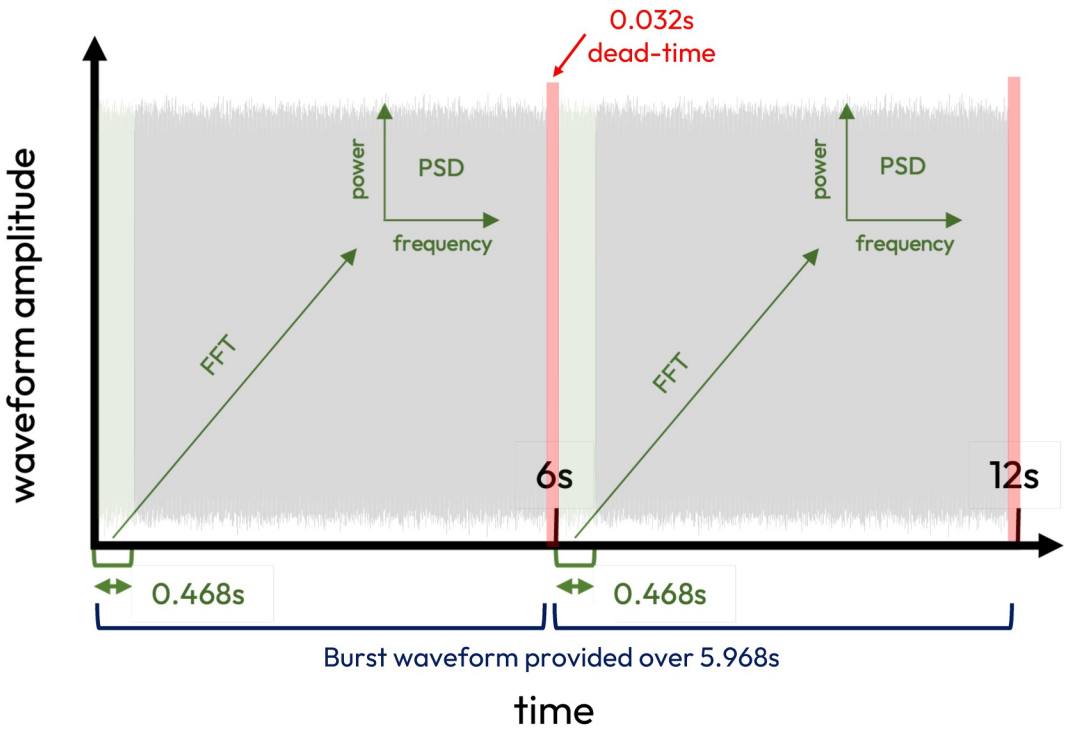

Figure 1. Schematic depicting how the survey magnetic and electric field data products are determined from raw waveforms. Every 6 s, the first 0.468 s subsection (beginning at the recorded timestamp) of the raw waveform is used as representative of the full 5.968 s duration. A single FFT is performed over this 0.468 s sample, and the results rebinned in frequency according to the semi-logarithmic bins specified in Kletzing et al. (2023).

2.1. EMFISIS Onboard Processing

The EMFISIS waves instrument took waveform measurements of the 3D electric and magnetic fields (Eu, Ev, Ew, Bu, Bv, Bw) with a sampling rate of 35,000 samples/s (Kletzing et al., 2013). These measurements were then processed on board the spacecraft, and a 3D power spectral density (PSD) for both the electric and magnetic field was sent down every 6 s to make up the frequently used "survey" data set.

Notably, the PSD available at each 6 s timestamp in the survey data is calculated from only the initial 0.468 s of waveforms within that time frame, with the timestamp on each data entry marking the interval start time. Figure 1 provides a schematic describing this onboard process over a 12 s period. A fast Fourier Transform (FFT) is applied over the time period $0 < t < 0.468$ s to obtain a PSD in linear frequency bins. This is then re-binned in semi-logarithmic frequency bins, as defined in Kletzing et al. (2023). This PSD is provided as the data entry at time 0.000 s, and this procedure is repeated at $6.000 < t < 6.000 + 0.468$ s for the entry at 6.000 s, and so on every 6 s. This means that the waves captured by the survey product are temporally resolved only above the 0.468 s scale, and then, in fact, only at 6 s intervals. However, some plasma waves in the magnetosphere, including whistler-mode chorus emissions, show temporal variability on much shorter timescales (e.g., Li, Bortnik, et al., 2011; Santolík, Gurnett, et al., 2003; Santolík et al., 2014; Zhang et al., 2018). The discrete structure of these waves is often characterized by rising and falling frequency tones (e.g., Li, Thorne, et al., 2011; Shue et al., 2019; Tao et al., 2012).

2.2. Burst-Mode Data Processing

In addition to the survey-mode, a second measurement scheme, known as the burst-mode, provided the full set of three-dimensional electric and magnetic field waveform measurements within the 5.968 s duration. This provides an opportunity to analyze the wave data, particularly the power variability, at a rate of up to 35 kHz resolution. However, this high-resolution data was not downloaded continuously (due to the high data volume), but sporadically (Kletzing et al., 2023). The burst-mode was preferentially triggered (Kletzing et al., 2023; Němec et al., 2022) at apogee, when large fluctuations in the magnetic field PSD were detected in a predefined frequency

range, typically between ($0.1f_{ce} < f < 0.7f_{ce}$), and at perigee, when large fluctuations in the magnetic field PSD were detected in the magnetosonic wave frequency range ($f < f_{LHR}$).

To create the burst PSD, each 5.968 s burst record of Bu, Bv, and Bw, which consists of 208,896 samples, is split up into 1024-point segments (~0.03 s). Each 1024 point time series is multiplied by a Hanning window function to ensure that the waveform within each segment is effectively periodic (Paschmann & Schwartz, 2000). A Fast Fourier Transform (FFT) is then applied to project the signal into the frequency domain. To obtain the true signal from the waveform receiver, the FFT must be multiplied by frequency dependent calibration coefficients that account for the instrument response. A table of coefficients is provided in the L2 data (Kletzing et al., 2013). According to Parseval's theorem (Paschmann & Schwartz, 2000), to obtain the PSD, for all positive frequencies, the absolute value is taken and squared, and then divided by the FFT frequency bandwidth. We also multiply by 2 to account for taking only positive frequencies.

When working with spacecraft data, the period of the measured waveforms will most likely not fit the continuity criteria during the sampling window. Therefore, a correction can be applied to account for the spectral leakage as a result of 'forcing' the signal to be periodic by using a window. The correction used in this work (Equation 1) is taken from Paschmann and Schwartz (2000), where N is the number of points, $w[j]$ is value of the window at each point, and W_{ss} is the fractional power loss from the PSD due to windowing. Therefore, for an estimate of true power, the FFT is divided by this correction.

$$W_{ss} = 1/N \sum_{j=0}^{N-1} w[j]^2 \quad (1)$$

The upper frequency limit on the power spectral density is set at 12 kHz, to match the upper limit imposed on the survey product. We have verified our processes on 0.468 s waveform samples that were sent down every 15 min as a procedural check that on-board algorithms were working correctly. This also provided samples throughout the orbit that were not biased toward large events to show that we can accurately reproduce the survey-mode results to high precision.

As well as the EMFISIS survey-mode PSDs and burst-mode waveforms, a number of other data products were required for the analysis. We use wave propagation properties provided in the L4 data, which have been calculated via the Singular Value Decomposition (SVD) method (Santolík, Parrot, & Lefeuvre, 2003). For the local magnetic field required to calculate the gyrofrequency, f_{ce}, we used the 1s resolution fluxgate magnetometer data aboard the Van Allen Probes. Estimates of the plasma frequency, f_{pe}, were provided in the L4 data, as determined by Kurth et al. (2015). The authors of this data set note that there are data gaps for a variety of reasons. Of all chorus-containing samples investigated in this study (and with the knowledge that the chorus identification in part depends on measurements of the plasma density, as will be detailed below), ~0.01% do not have an associated plasma density. When AE and f_{pe}/f_{ce} are considered as parameters together, these samples are omitted.

2.3. Identifying Chorus Waves

The survey spectra were used to identify chorus waves. If a burst sample was taken at the same time step as a positive survey identification, the burst sample was also classified as containing a chorus wave. In order to identify whistler-mode chorus events, wave measurements must satisfy particular criteria. First, chorus waves must have wave properties consistent with the whistler-mode solution of the dispersion relation (Stix, 1992). More specifically, and similar to other studies identifying such waves (e.g., Bingham et al., 2018; Hartley et al., 2018, 2019, 2023; Li et al., 2014; Li et al., 2016), chorus must have a planarity >0.6, ellipticity >0.7 and polarisation >0.5. In line with previous definitions (Tsurutani & Smith, 1974), the emissions are assumed to lie within the frequency range between $f_{LHR} < f < 0.9f_{ce}$, where f_{LHR} is the lower hybrid resonance frequency, and f_{ce} is the local electron gyrofrequency.

Second, the true wave signal must be separated from the background noise on the instrument. We performed a background subtraction on the EMFISIS survey measurements using a similar method to that described in Malaspina et al. (2017). For each frequency band, f_n, between 2.1 Hz and 11.2 kHz, the three-dimensional magnitude of the magnetic field PSD measurements were compiled into distributions of counts against PSD value. For each distribution, we fitted a Gaussian, and a signal threshold, $PSD_{th,n}$, was set at 2 standard deviations

from the mean of the distribution ($\langle PSD \rangle_n$), in each frequency band. Malaspina et al. (2017) perform this threshold fitting for only the lowest frequency band, and then take $PSD_{th,n} = \langle PSD \rangle_n + \left(PSD_{th,0} - \langle PSD \rangle_0\right)$ as the threshold in each subsequent band. This is a conservative estimate, as the Gaussian fit to the distributions become narrower as frequency increases. Therefore, this method could result in a fraction of the wave power being removed, particularly in higher frequency bands. By performing the fit independently for each frequency band, we hope to maximize the wave power found. A comparison in the resulting "EMFISIS signal-to-noise thresholds" for each method is presented in Figure S1 of Supporting Information S1.

Finally, the type of whistler-mode wave that will be observed by a spacecraft is highly dependent on the plasma density. Within the magnetosphere, chorus waves exist in lower plasma densities, known as the plasma trough ($\sim$1 cm^{-3}) (McPherson & Koons, 1970), whilst in the higher density region of the plasmasphere ($\sim$100 cm^{-3}), hiss waves are the dominant emission (Thorne et al., 1973). There are a number of methods in the literature by which the plasmasphere is identified. In this study, we have tried to maximize the number of positive chorus identifications by combining together various methods of plasmapause identification. The details of this optimization are given below.

2.3.1. Identifying the Plasmapause

The motions of cold plasma within the plasmasphere are controlled by the interplay between Earth's convection and corotation electric fields. Given that the co-rotating electric field remains essentially constant in time, changes in the solar wind, and therefore the convective dawn-dusk electric field, control the spatial extent of this region (Koskinen & Kilpua, 2022). For example, under active conditions, the convective electric field will increase and the plasma will be eroded as a result of the enhanced ExB drifts. This erosion creates a sharp electron density boundary, called the plasmapause, between the plasmaspheric particles, and the higher energy particles of the plasma trough whose motion is governed by the dipole magnetic field (Carpenter, 1963, 1966).

There are three main methods by which one can distinguish between measurements taken in the plasmasphere and the plasma trough in spacecraft data. Below, we describe all three and their associated drawbacks. We will then present our method of combining these techniques, and a breakdown of the plasmapause "type" statistics.

1. *Density gradient criteria*. Often the plasmapause appears as a sudden and obvious density drop, or "knee" (Carpenter, 1963). For our study, using the definition by Moldwin et al. (2002), a density drop of a factor of 5 or larger within 0.5L^* was required to identify a "gradient-associated" plasmapause, $L_{pp,grad}$, on a given half orbit. On each half-orbit, the plasmapause crossing was taken to be at the low-density end of the gradient identified closest to perigee. Half-orbits with double crossings (opposing positive and negative gradients) were excluded, as these likely indicate passage through a plasmaspheric plume. The plasma density is available in the L4 data of the EMFISIS instrument, as inferred by Kurth et al. (2015) through identification of waves at the upper hybrid resonance frequency, f_{UHR}, in the electric field PSD, or, when the latter are not present, the low frequency cut-off of electromagnetic continuum radiation. There are timestamps, however, for which no density data was provided by this algorithm. This was either due to ECH wave contamination of the f_{UHR} line, uncertainty when f_{UHR} goes below 10 kHz, or human error, as each algorithm "failure" was checked manually. During these times, the gradient criterion cannot be used.
2. *ECH wave criterion* Whilst ECH waves may interfere with the density estimations on the Van Allen Probes, Meredith et al. (2009) suggested that ECH waves also terminate at the plasmapause and can therefore be used as indication of the boundary. However, X. Liu et al. (2020) found that two categories of ECH wave may exist; one that terminates at the plasmapause, and a second that may propagate into the plasmasphere, mainly in the first harmonic. The latter are far fewer in occurrence and predominantly on the night-side. In this study, ECH waves are identified in the electric field PSDs if any emissions were found between $2f_{ce} < f < 3f_{ce}$, following a background subtraction via the same method as was described earlier for the magnetic field PSDs. The first harmonic is omitted to avoid the latter category of ECH wave that can propagate into the plasmasphere. The upper frequency bound can creep outside of the WFR receiver range, and in these cases the electric field measurements from the HFR receiver were used. There are two minor caveats associated with this criterion. First, the HFR is limited to measurements along a single axis only, meaning that some ECH waves extending into this frequency range may not be detected. Second, the spatial distribution of ECH waves may introduce an MLT bias in the chorus identification near post-midnight and dawn (see spatial distributions, e.g., in Meredith

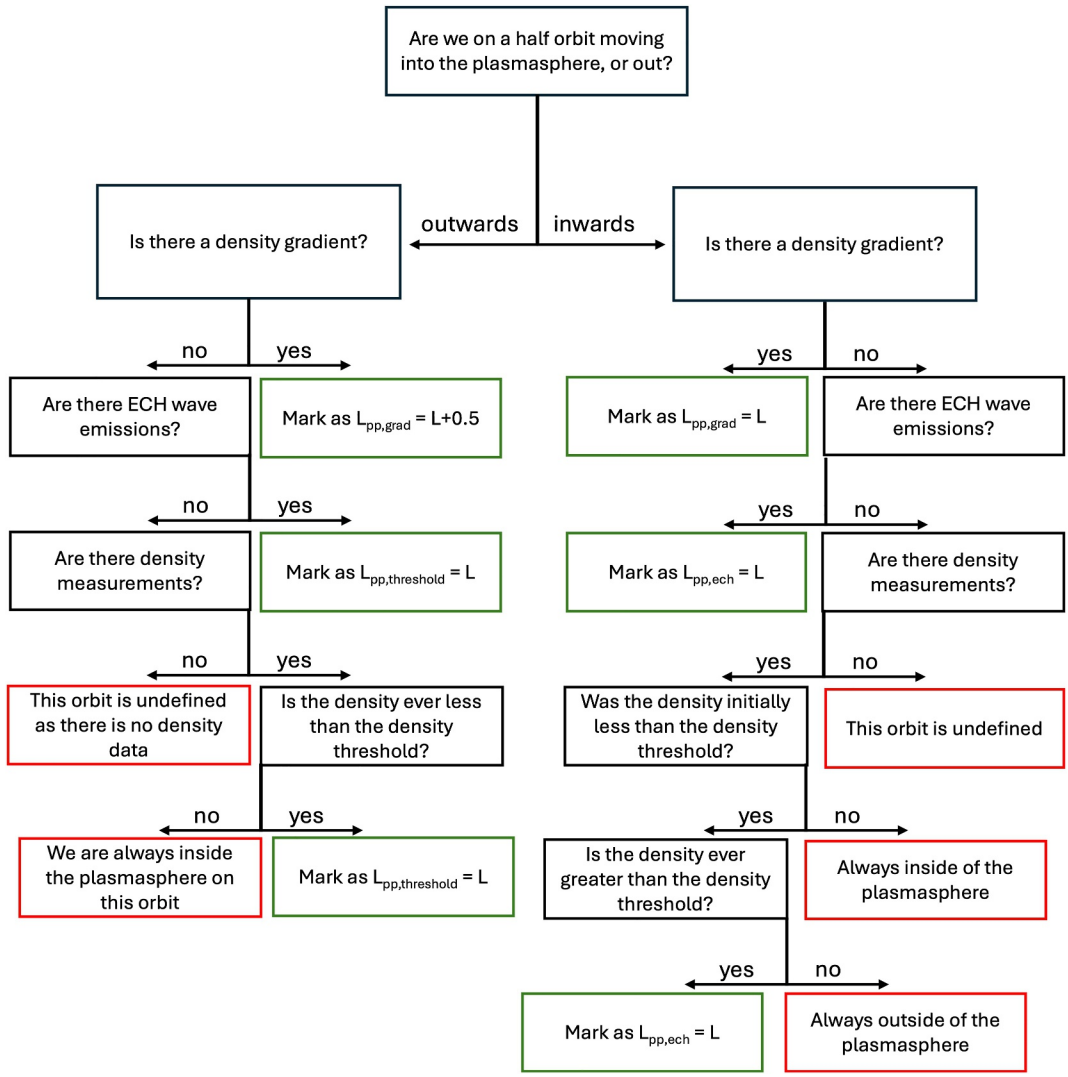

Figure 2. A flowchart depicting the algorithm used to identify the plasmapause according to the criteria defined in Section 2.3.1.

et al. (2009), Zhou et al. (2023)). However, this potential bias is largely mitigated by combining all three identification methods, given that the other two are not affected by this issue.

3. *Density threshold criterion* When moving from inside to outside of the plasmasphere, the density can drop far more gradually than is required by the density gradient method, particularly during quiet times. In fact, from the Van Allen Probes perspective, Ripoll et al. (2022) suggested that the density 'knee' does not exist for up 47% of the satellite orbits. To account for this, a plausible absolute density between 30−100 cm^{-3} is often used as an alternative (e.g., Hartley et al., 2018; Thaller et al., 2015; Tyler et al., 2019b). Another option would be to use an empirical model with respect to L based upon the density gradient criteria. For example, Sheeley et al. (2001) used CRRES observations to derive $n_{pp,\text{Sheeley}} = 10(6.6/L)^4$ as a density threshold for the plasmasphere. In our study, we follow the method by Li, Thorne, Bortnik, et al. (2010) and take the maximum of $n_{pp,Sheeley}$ and 50 cm^{-3} to estimate the plasmapause density threshold ($L_{pp,threshold}$).

In order to balance maximizing the number of chorus wave events found in the survey data, with having confidence in knowing whether we are in- or outside of the plasmasphere, a combination of these three methods was used to identify which region the spacecraft was in. A flow diagram of the algorithm used is shown in Figure 2, with the "density gradient criteria" used as first preference, then moving onto the "ECH wave criteria" if this was unsatisfied, and finally using the "density threshold criteria" as the final option. Each half orbit is treated

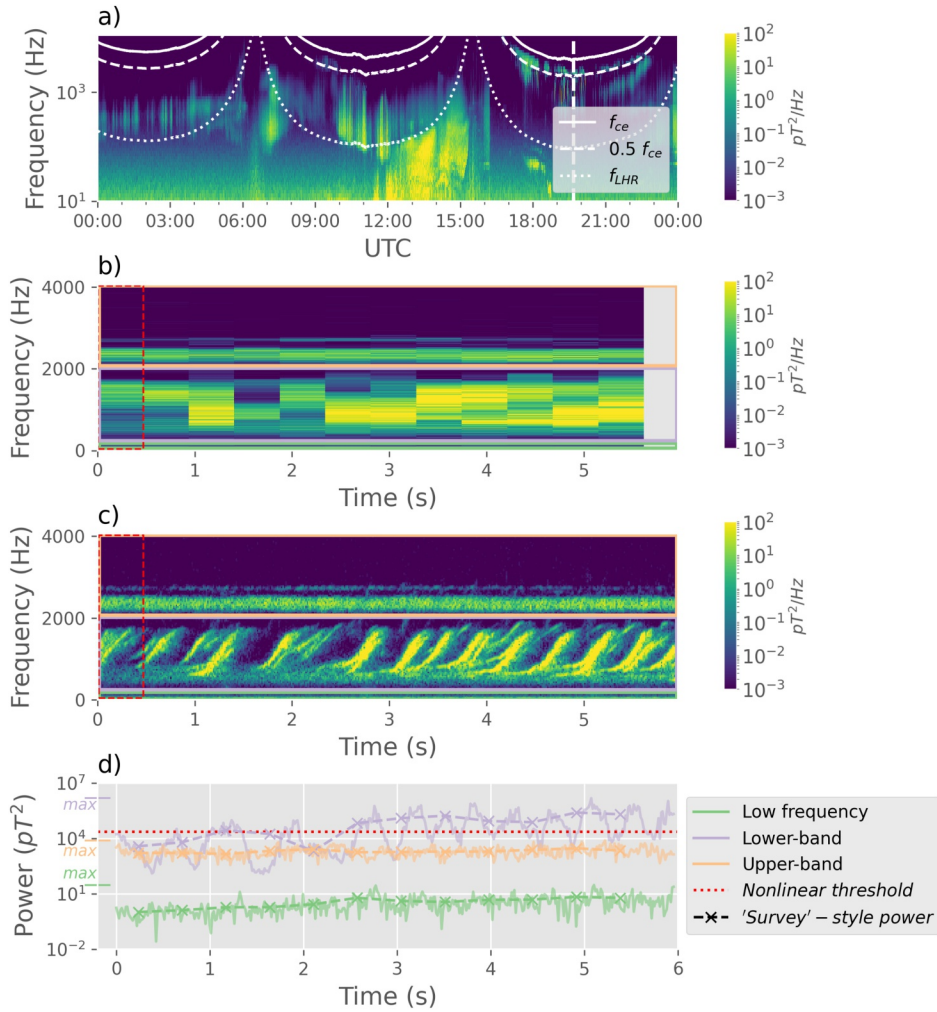

Figure 3. (a) Survey magnetic field PSD for example, date and time (2016-01-20). The solid, dashed, and dotted white lines show local f_{ce}, $0.5\,f_{ce}$, and f_{LHR}, respectively. The vertical white line marks the timestamp (19:23:21.9846861) of an identified chorus-containing sample. (b) Shows the burst waveforms at the given timestamp converted to PSDs following the procedure in Kletzing et al. (2023) on-board the Van Allen Probes. The sub-sample used as the "survey-mode" spectra at the given timestamp is shown in the red dashed box. The green, purple and orange boxes indicate the frequency ranges of low frequency, lower-band and upper-band chorus, respectively, used in this study. (c) Shows the burst PSD as processed as described in Section 2.2., again with the colored boxes indicating the frequency range. (d) Shows line plots of the integrated power in each chorus frequency range over the 5.968 s burst record. The dashed red line is an indicative estimate of a nonlinear power threshold.

independently, however, in the cases where there was adequate density data but no gradient or threshold criteria was satisfied, and no ECH waves were detected, the full orbit was considered to have remained inside the plasmasphere. In the cases where there was not adequate density data, and no ECH waves were detected, the orbit was classed as "undefined".

2.4. Survey-Mode and Burst-Mode Sampling and Chorus Occurrence

In this study, the selection of whistler-mode chorus waves identified a total of 14,455,656 chorus-containing timestamps in the survey data set, of which there were 749,352 (~5%) matching samples in the burst data set for Van Allen Probe A and B. An example of the PSDs for an identified chorus-containing sample from the survey and burst data sets is shown in Figure 3.

Figures 4a and 4b show the number of samples in the equatorial region ($|\lambda_m| < 6°$) as a function of L^* and MLT for the survey and burst data respectively. The plots use data from both satellites and bins with samples less than 50 are excluded. The fraction of burst sampling to survey sampling is shown in Figure 4c. There is a smaller

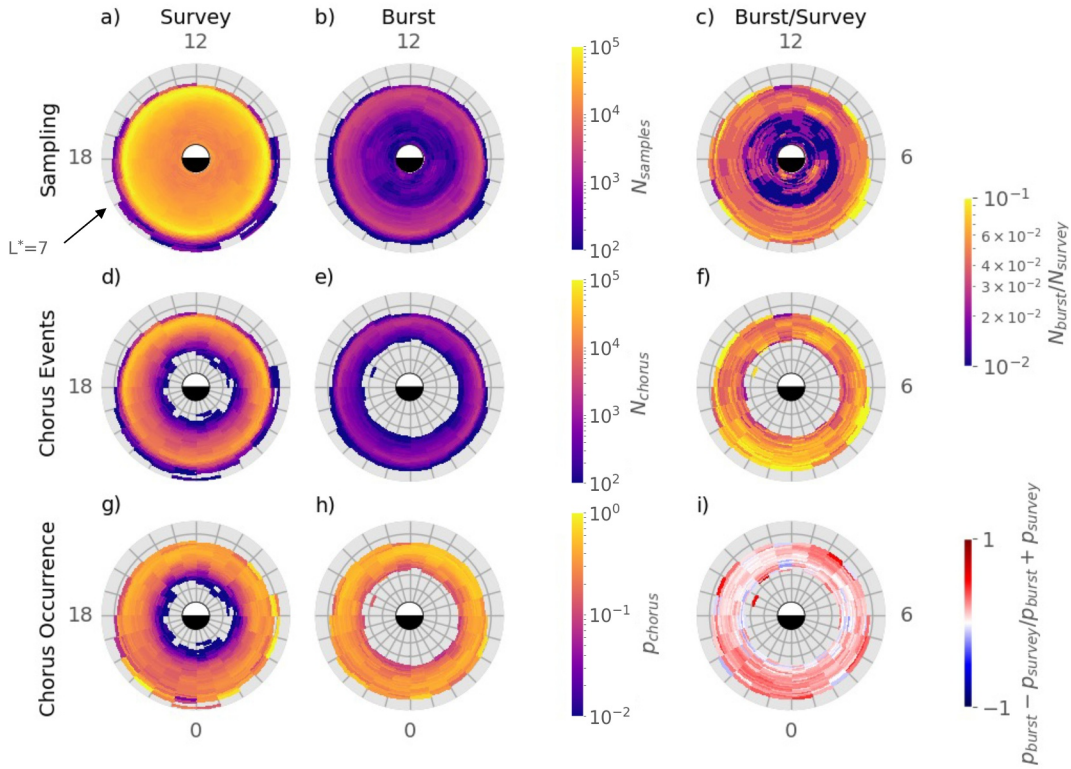

Figure 4. For equatorial latitudes ($|\lambda_m| < 6°$), sampling counts from the EMFISIS instrument ($N_{samples}$) for the (a) survey and (b) burst data sets; detected chorus events (N_{chorus}) for (d) survey and (e) burst data sets; and the normalized probability of a sample containing a chorus event in each (ML T, L^*) bin for (g) burst and (h) survey data sets. The ratio (N_{burst}/N_{survey}) for samples and chorus events is plotted in panels (c, f), respectively. The normalized difference in chorus probability, $(p_{chorus,burst} - p_{chorus,survey})/(p_{chorus,burst} + p_{chorus,survey})$, in each (MLT, L^*) bin is given in panel (i).

burst-to-survey relative data coverage for small L^*, between $1 < L^* \leq 3.5$, as compared to $3.5 < L^* \leq 5.5$. The burst-to-survey relative coverage in MLT also remains almost uniform between $3.5 < L^* \leq 5.5$ For instance, for all 0.1 L^* bins within this range at equatorial latitudes, the standard deviation in the sampling ratio across all MLTs was between 10 and 24%, whilst it was between 34 and 100% below $L^* \leq 3.5$. Similarly, at off-equatorial latitudes, the standard deviation was between 6 and 35% for $3.5 < L^* \leq 5.5$, and 29–117% below $L^* = 3.5$. Below $L^* = 3.5$, the spacecraft will often be inside the plasmasphere where chorus waves are not generated. However, within range $3.5 < L^* \leq 5.5$, the spacecraft will mostly be within the heart of the radiation belts, and therefore the burst-mode has sufficient sampling of our particular region of interest.

Figure 4d shows the number of chorus events identified in the survey data, N_{cs}, and Figure 4e shows the number of burst samples present when chorus is identified in the survey data, N_{bcs}. The ratio N_{bcs}/N_{cs} is shown in Figure 4f.

From Figure 4d, we can see that chorus events mainly occur within the outer L^* range of the Van Allen Probe orbit, between $4 < L^* \leq 6$, and therefore there is adequate burst coverage within the regions of interest. If one wanted to perform a similar study using burst-mode for analyzing other plasma emissions observed in the Van Allen Probe orbit, for example, with plasmaspheric hiss, greater care might be required before drawing statistical conclusions.

The chorus occurrence probabilities were calculated by taking $p_{chorus} = N_{chorus}/N_{samples}$ for each data set, and the normalized difference in probability of chorus occurrence is defined as $(p_{chorus,burst} - p_{chorus,survey})/(p_{chorus,burst} + p_{chorus,survey})$. The difference in occurrence probability between the survey and burst-mode data sets shows some preference by the chorus identified in the burst-mode toward the night side for most L^*, as seen in Figure 4i. However, the mean difference in chorus occurrence probability across all MLTs was ~0.12, showing that the burst coverage can be used as a representative subset of the chorus regions observed by Van Allen Probes.

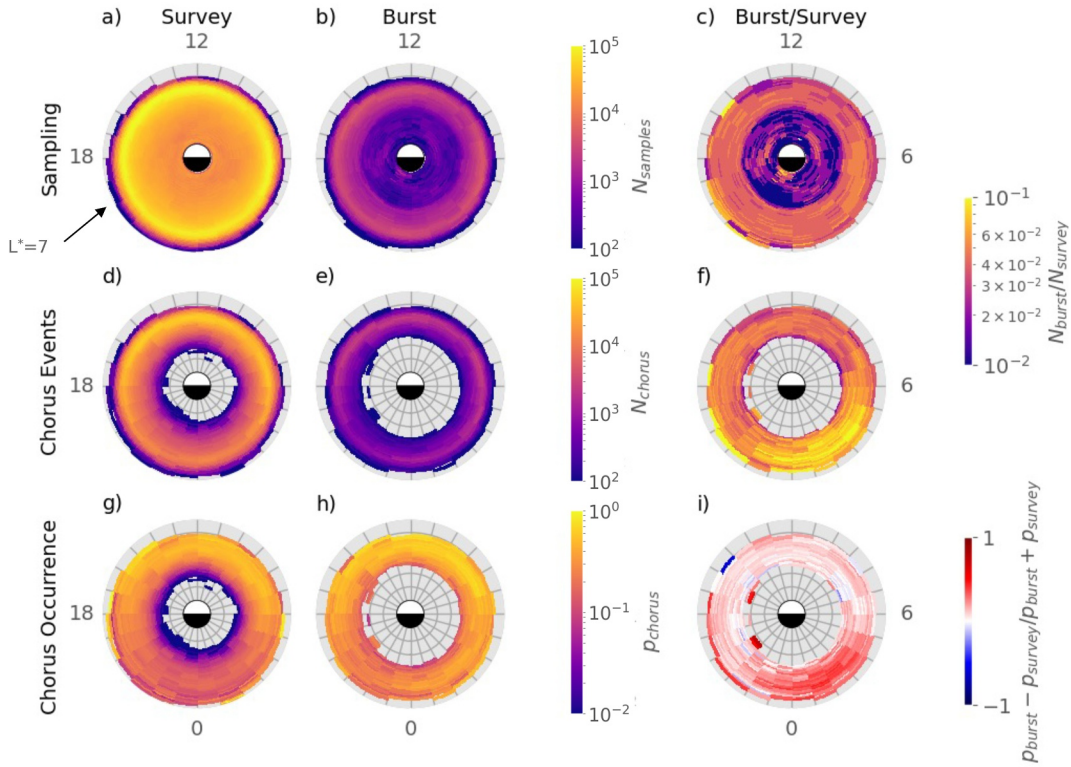

Figure 5. For off-equatorial latitudes ($|\lambda_m| \geq 6°$), sampling counts from the EMFISIS instrument ($N_{samples}$) for the (a) survey and (b) burst data sets; detected chorus events (N_{chorus}) for (d) survey and (e) burst data sets; and the normalized probability of a sample containing a chorus event in each (MLT, L^*) bin for (g) burst and (h) survey data sets. The ratio (N_{burst}/N_{survey}) for samples and chorus events is plotted in panels (c, f), respectively. The normalized difference in chorus probability, $(p_{chorus,burst} - p_{chorus,survey})/(p_{chorus,burst} + p_{chorus,survey})$, in each (MLT, L^*) bin is given in panel (i).

The same procedure was repeated for off-equatorial sampling, and the results are shown in Figure 5. Similarly to the case of equatorial sampling, the mean difference in chorus occurrence probability across all MLTs was ∼0.13. further supporting the burst-mode provides a good representation of survey-mode sampling.

2.5. Survey-Mode and Burst-Mode Chorus Power Comparison

We first compared statistics of total chorus power for all chorus-containing samples found in the survey, against the statistics of total chorus power for the burst subset. To obtain the total powers, each chorus event was integrated in frequency between the bounds of ($f_{LHR} \leq f < 0.9f_{ce}$). For fair comparison and to ascertain whether any bias had been introduced by the burst-mode's "triggered" data collection, the integrated burst FFTs were first averaged over the survey 5.968 s for each chorus-containing sample, such that we had a burst power average for the 6s timestamp. We could then construct total power distributions for each data set by binning in MLT, L^* and MLAT.

Figures 6 and 7 show the distribution of power for all identified chorus-containing samples for the equatorial and off-equatorial events respectively. The panels in Figures 6a, 6b and 7a, 7b show the mean power in each MLT and L^* bin for all of the chorus events for survey and burst respectively, whilst Figures 6c, 6d and 7c, 7d show the corresponding normalized power ($P_{average} \times p_{chorus}$) in each bin for survey and burst respectively.

Figures 6a–6d show that when the spacecraft was at equatorial latitudes, the chorus waves were strongest in the post-midnight sector, between 0 and 6 MLT. Moving to higher latitudes, Figures 7a–7d show that the chorus wave power persisted in this region, but also spread out toward the morning sector, around 6–12 MLT.

Both Figures 6 and 7 show that the average power for the burst samples was higher than that of the survey. Given that the burst chorus samples are a subset of the survey, this suggests that, even if the sampling distribution was

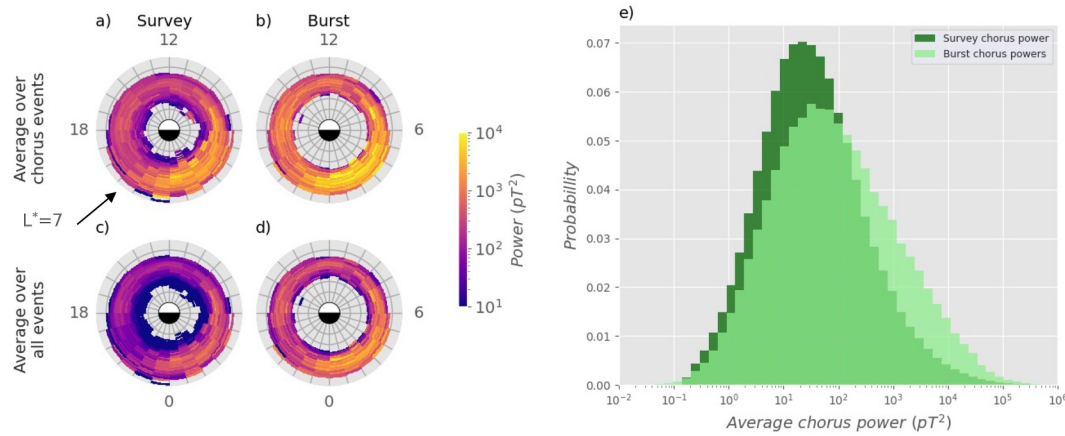

Figure 6. For equatorial latitudes ($|\lambda_m| < 6°$), average chorus wave power over chorus events for (a) survey and (b) burst data sets; average chorus wave power over all sampling for (c) survey and (d) burst data sets; and (e) The probability distribution of chorus power in the survey and burst data sets.

mostly uniform across MLT and L*, burst-mode was consistently sampling from the higher-power chorus populations. Additionally, because the burst had (on average) higher occurrence probabilities, as seen in Figures 4e and 5e, the normalized chorus power is much higher for the burst chorus events in the central chorus regions around $L = 4$. However, large numbers of bins on the outer and inner boundaries of the chorus region for the burst subset had fewer samples than our minimum bin requirement (50 samples), resulting in a narrower distribution in L*.

The histograms in Figures 6e and 7e show the total distribution of power in all burst and survey samples, respectively. The samples have been logarithmically binned between 10^{-2} and 10^{6} pT^2. From these histograms, it's clear that for both the equatorial and off-equatorial populations, the burst subset shows a higher probability of the power in a sample being $>10^2$ pT^2. However, the range of chorus powers was roughly the same across both distributions, between 10^{-1} $pT^2 < P < 10^6$ pT^2. Therefore, burst samples are not constrained to high-amplitude waves only. A further breakdown of the histograms by MLT and L* are provided in Figures S2 and S3 of Supporting Information S1 for equatorial chorus, and in Figures S4 and S5 of Supporting Information S1 for off-equatorial chorus in the Supporting Information S1.

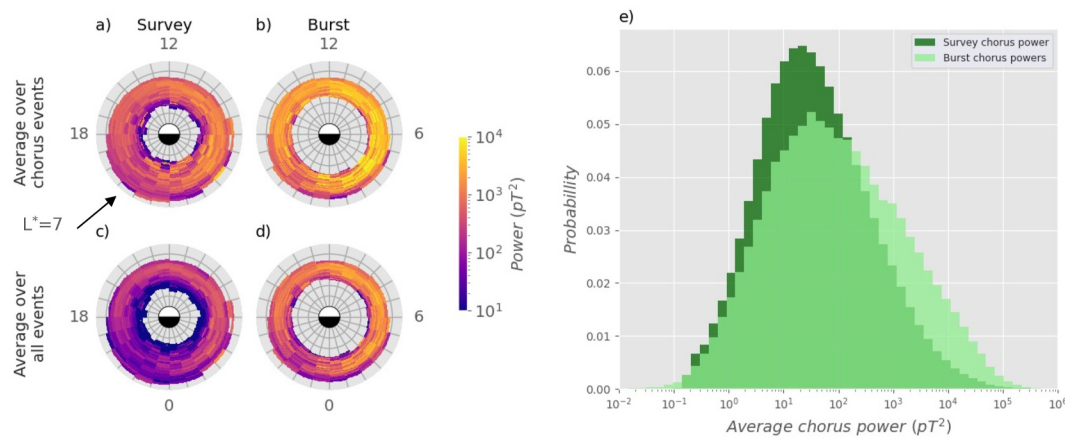

Figure 7. For off-equatorial latitudes ($|\lambda_m| \geq 6°$), average chorus wave power over chorus events for (a) survey and (b) burst data sets; average chorus wave power over all sampling for (c) survey and (d) burst data sets; and (e) the probability distribution of chorus power in the survey and burst data sets.

Table 1
Table of Co-Occurrence of Different Spectral Chorus Types Among Detected Chorus Waves

	LF only	LB only	UB only	LF & LB	LB & UB	LF & UB	LF & LB & UB	Total
$\lvert\lambda_m\rvert < 6°$	13.93%	10.22%	4.09%	30.07%	7.34%	1.60%	6.03%	73.28%
$\lvert\lambda_m\rvert \geq 6°$	4.68%	5.02%	0.26%	14.03%	0.81%	0.18%	1.73%	26.72%

3. Chorus Power and Its Variability

From now on, all statistics are for the chorus events identified in the survey-mode data set that had a corresponding burst-mode record only. Therefore, the statistics presented describe times only when we have simultaneous and co-located burst and survey records. Subsequent comparisons made between survey- and burst-mode powers are therefore direct one-to-one comparisons between the two data-capture modes operating concurrently.

3.1. Power and Variability of Low Frequency, Lower-Band and Upper-Band Chorus

The events were then divided into three frequency bands, and the burst and survey PSDs were integrated between the following bounds; Low Frequency (LF, with range $f_{LHR} \leq f < 0.1f_{ce}$); Lower-Band (LB, with range $0.1f_{ce} \leq f < 0.5f_{ce}$); and Upper-Band (UB, with range $0.5f_{ce} \leq f < 0.9f_{ce}$), as defined in Figure 3. It is interesting to note how often we see each type of band over the Van Allen Probes' orbits. The event list can be broken down into different combinations of chorus frequency ranges, with the percentage of samples in each combination presented in Table 1. We emphasize that these percentages are derived from samples only when at least one chorus type is observed; and is thus a conditional distribution. All further comparison between chorus waves observed in different frequency ranges are with respect to these populations.

From this it is clear that the most common spectral combination was low frequency and lower-band waves together. Additionally, upper-band chorus was almost never observed without lower-band chorus. Both of these statistics agree with what is expected from current wave generation theories (e.g., Gao et al., 2016), as well as results from another observational study (Teng et al., 2019).

We choose to study the following parameters because they provide key information regarding the chorus power and its variability on short timescales. Additionally, they help to highlight the waves that could potentially violate the conditions required for the formal validity of quasilinear theory (Allanson et al., 2024), as discussed in the introduction. In particular, for each 5.968 s burst record, we record:

1. The survey power at the corresponding 6s timestamp, P_{survey}. This is calculated by integrating the standard survey data product in each frequency range. This is the "traditional" measurement of wave power, taken on timescales upon which global wave statistics are made and fed into quasilinear models.
2. Peak burst power over the 5.968 s duration, $P_{burst,max}$, for each frequency range. These show us the maximum powers that are reached, which cannot be resolved in survey-mode data sets. Additionally an understanding of where and when high-intensity waves are prevalent could indicate where nonlinear wave-particle interactions occur (Bortnik et al., 2008).
3. The ratio between the peak burst power and survey power for every simultaneous pair of individual burst- and survey-mode record, $P_{burst,max}/P_{survey}$, to infer the extent to which the peak burst power can exceed the survey power.
4. The ratio between the inter-quartile range of the power (difference between the 75th ($P_{burst,Q3}$) and 25th ($P_{burst,Q1}$) percentiles) and the median power ($P_{burst,Q2}$), which we shall call normalized inter-quartile range (IQR_{norm}) from now on. This parameter will help to characterize the variability of wave power over a small number of wave periods.

Finally, an approximate "high-power" threshold above which one may expect nonlinear wave-particle interactions to occur, is shown by the dashed red horizontal line in Figure 3d. First devised in Zhang et al. (2018) and Mourenas et al. (2018) by balancing the wave electromagnetic field force and the force on a particle due to background magnetic field, the threshold is dependent upon several properties of the field, waves and particles in question. In this case, the threshold was derived under the following assumptions: the interaction takes place in a dipolar magnetic field, in the heart of the radiation belts ($L \sim 4$–5), near equatorial latitudes; the waves propagate nearly parallel to the field and have a power spectrum peaking at lower-band chorus frequencies; and the particles

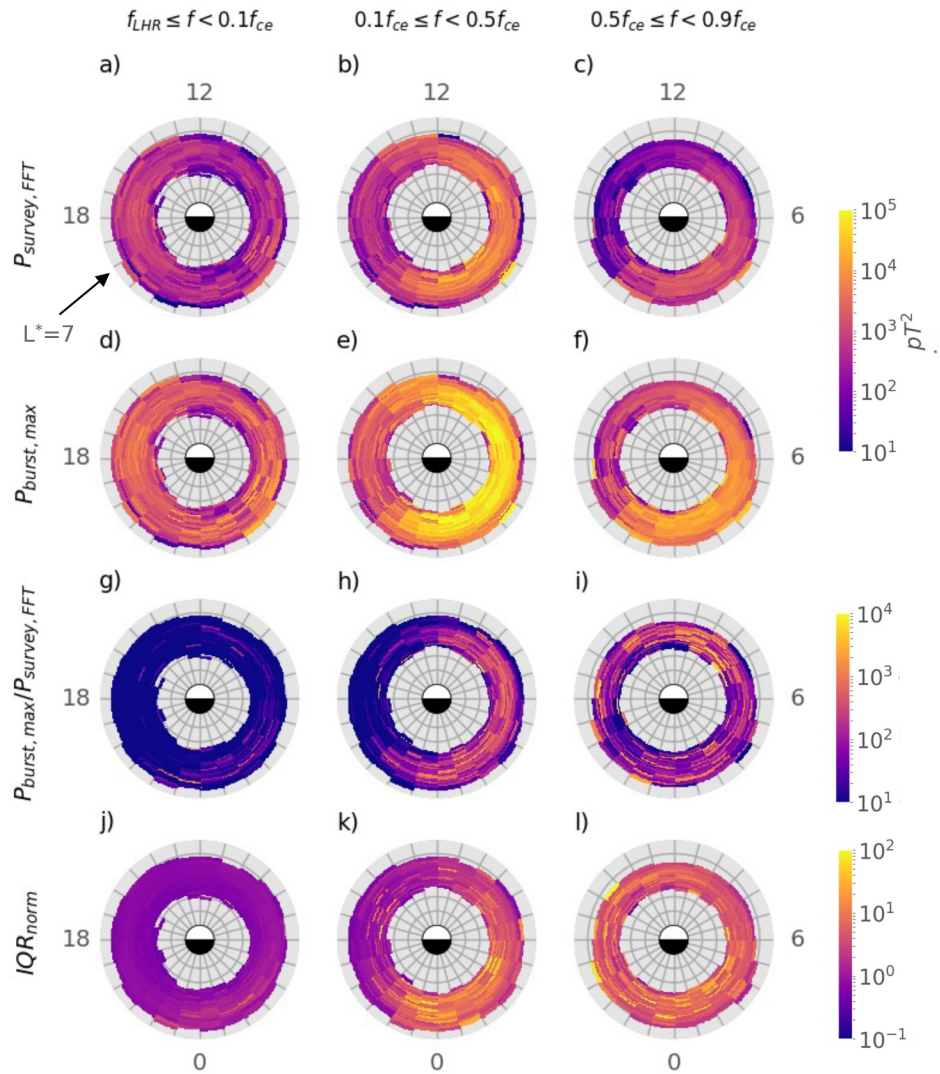

Figure 8. Chorus events in burst divided into low frequency, lower-band and upper-band for equatorial latitudes ($|\lambda_m| < 6°$). For each frequency range, the subpanels show (a–c) average chorus power for corresponding survey events; (d–f) maximum chorus power from burst events; (g–i) ratio between the maximum burst power and the survey power; and (j–l) the normalized inter-quartile range ($\frac{Q3-Q1}{Q2}$) for each burst sample.

are at equatorial pitch angles (~50–70°) and relativistic energies (~0.3–0.5 MeV). For the above parameters this corresponds to a threshold wave amplitude of about ≈120–160 *pT*. This threshold has since been used in Chakraborty et al. (2025) to indicate the presence of high-amplitude waves in Van Allen Probe data. Further evaluation of this technique can be found in the discussion.

It should be noted that only chorus-containing samples with power in a given band were included in the statistics for that band. For example, if chorus power was only observed in the lower-band for a given sample, that sample would not be included in the low frequency or upper-band statistics. In Figures 8 and 9, the mean of each statistic in a given MLT and L^* bin is calculated by averaging over the values for each individual burst (and corresponding survey) record in that bin. This is done for each of the three frequency bands for equatorial and off-equatorial chorus events, respectively.

From the analysis of both Figures 8 and 9, it is evident that the peak burst power is significantly larger than the corresponding survey power. For example, in both the equatorial and the off-equatorial populations, and all frequency ranges, the ratio never went below 10 in any (MLT, L^*) bin. Additionally, low frequency and lower-

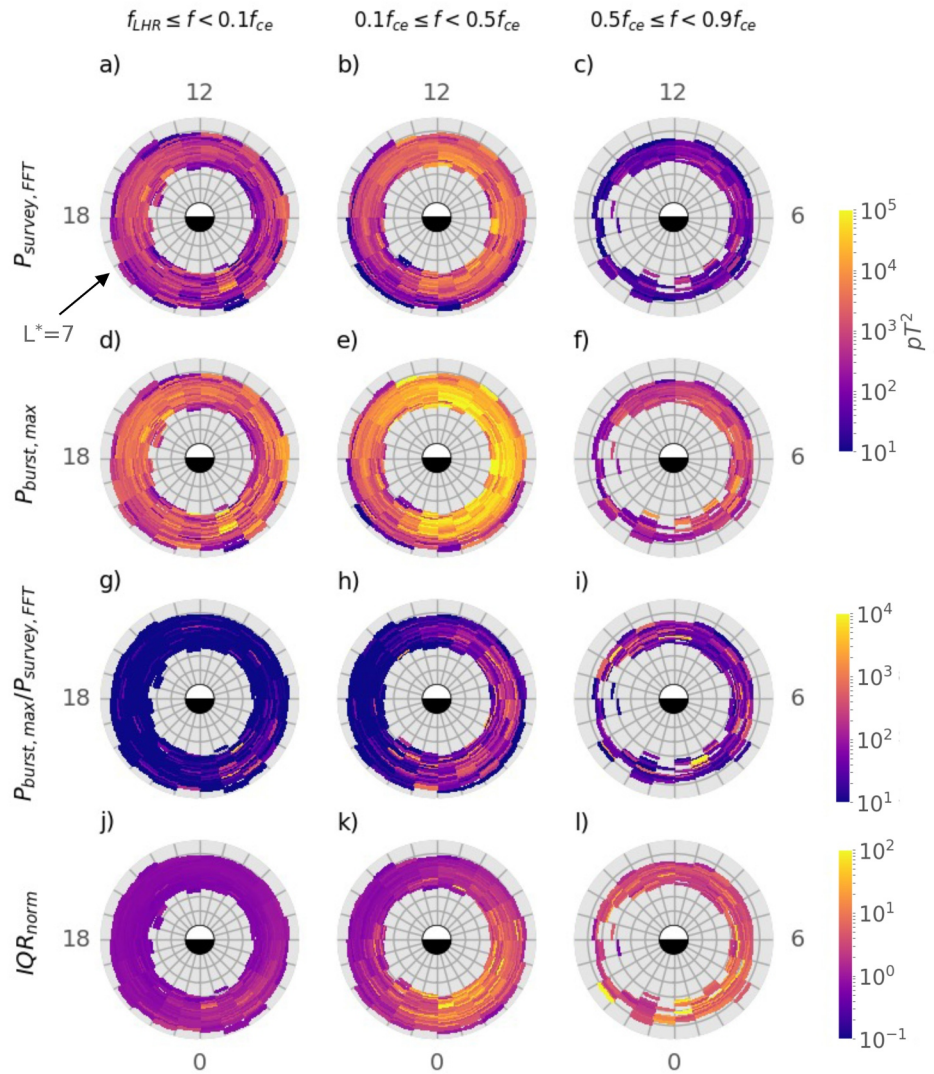

Figure 9. Chorus events in burst divided into low frequency, lower-band and upper-band for off-equatorial latitudes ($|\lambda_m| \geq 6°$). For each frequency range, the subpanels show (a–c) average chorus power for corresponding survey events; (d–f) Maximum chorus power from burst events; (g–i) ratio between the maximum burst power and the survey power; and (j–l) the normalized inter-quartile range ($\frac{Q3-Q1}{Q2}$) for each burst sample.

band chorus showed the largest ratio (>100) between the burst and survey distributions in the post-midnight and dawn sectors for both latitude ranges. Interestingly, across all (MLT, L*) bins in which chorus was observed, the upper-band chorus showed a consistent ratio (~100).

Additionally, from panel (j–l) in each Figure, for all chorus groups, the ratio between inter-quartile range and median was greater than 1—indicating that the spread of the middle 50% of data in each burst sample was always larger than the median value. A similar trend to that of the peak power-to-survey ratio was observed for both the lower-band and upper-band chorus; the IQR_{norm} was largest for the lower-band frequencies, in the regions between 0 and 6 MLT for equatorial events, and further extending between 0 and 12 MLT for off-equatorial events, whilst the upper-band chorus showed an almost constant IQR_{norm} across all MLTs and L*, with slightly larger values in the 0–6 MLT sector for off-equatorial cases.

These results show that lower- and upper-band chorus have a significant power variability below the 0.468s timescale upon which the survey-mode data set is determined. Furthermore, the average of the peak powers on this timescale in a given MLT and L* bin can be orders of magnitude larger than the average survey power. It is

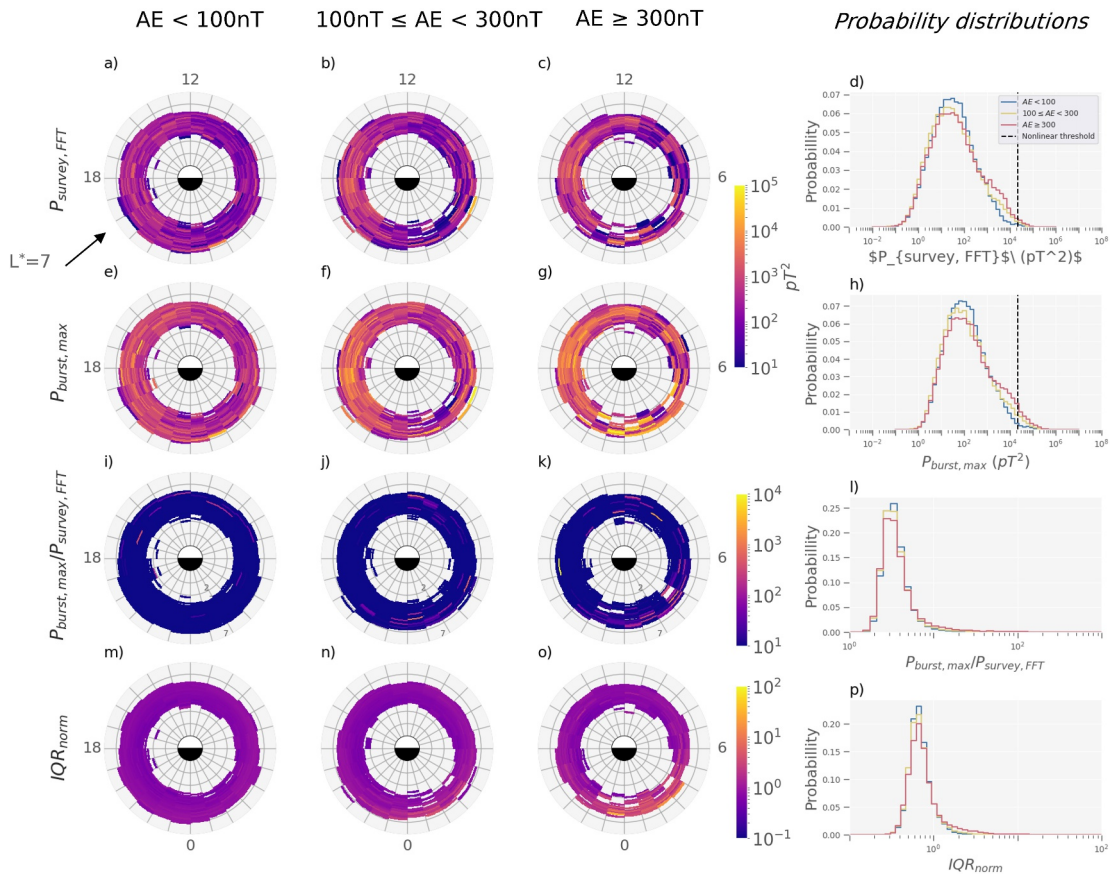

Figure 10. Low frequency chorus events at equatorial latitudes separated by activity into AE $<$ 100 nT, 100 nT $\leq$ AE $<$ 300 nT, and AE $\geq$ 300 nT. The sub-panels show the same statistics as before, with (a–c) average chorus power of survey events for which a burst record exists; (e–g) maximum chorus burst power; (i–k) ratio between the maximum chorus burst power and the survey power; and (m–o) $\frac{Q3-Q1}{Q2}$. Additionally, (d, h, l, p) show the probability distributions of survey power, peak power, power ratio, and the IQR_{norm} for these events, respectively. An estimate of a high-power threshold is given by the dashed red line on (d) and (h).

important to note, using Table 1, that whilst the underlying variability appears most dramatic for upper-band chorus, upper-band chorus was only observed for ∼22% of the chorus samples, whilst lower-band chorus was observed in over 78% of chorus samples.

We now proceed to further analyze these aggregated statistics by breaking them down with respect to activity index, AE, in Section 3.2 and f_{pe}/f_{ce} in Section 3.3. We would like to emphasize that the "triggered" burst-mode did not skew the chorus statistics toward active conditions. The probability distribution of AE values across all chorus-containing burst records is shown in Figure S7 of Supporting Information. From these, the activity ranges with the largest number of samples were below 100 nT (during quiet times).

3.2. Dependence on AE

The AE geomagnetic activity index was chosen because it is often associated with substorm activity and chorus wave generation (Jaynes et al., 2015; Meredith et al., 2001; Tsurutani & Smith, 1974). Additionally, and for this reason, the AE index has repeatedly been used to parameterize chorus wave models (Aryan et al., 2014, 2020; Agapitov et al., 2019; Li, Bortnik, et al., 2011; Meredith et al., 2012), including those that are fed into radiation belt models (e.g., Aryan et al., 2021; Meredith et al., 2001, 2012, 2020).

From now on, we shall focus on the events at equatorial latitudes. The events were separated into three activity levels, using the AE index supplied as 1-min averages; AE $<$ 100 nT, 100 nT $\leq$ AE $<$ 300 nT, and AE $\geq$ 300 nT. The results are shown in Figures 10–12 for each of the three frequency ranges, respectively. For each activity, the rows show, from top to bottom, P_{survey}, $P_{burst,max}$, $P_{burst,max}/P_{survey}$ ratio and IQR_{norm}, respectively. Additionally, the probability distribution for each statistic is given at the end of each row. For each

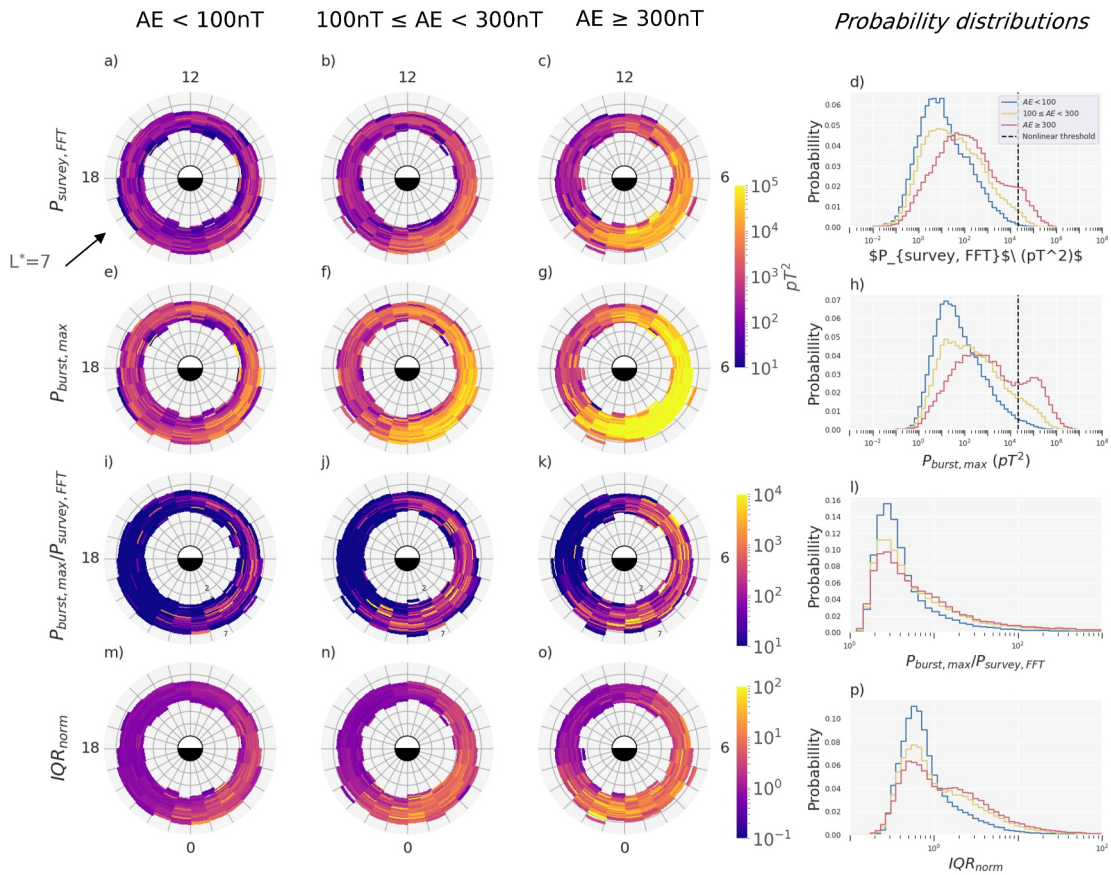

Figure 11. Lower-band chorus events at equatorial latitudes separated by activity into AE $<$ 100 nT, 100 nT $\leq$ AE $<$ 300 nT, and AE $\geq$ 300 nT. The sub-panels show the same statistics as before, with (a–c) average chorus power of survey events for which a burst record exists; (e–g) maximum chorus burst power; (i–k) ratio between the maximum chorus burst power and the survey power; and (m–o) $\frac{Q3-Q1}{Q2}$. Additionally, (d, h, l, p) show the probability distributions of survey power, peak power, power ratio, and the IQR_{norm} for these events, respectively. An estimate of a high-power threshold is given by the dashed red line on (d, h).

combination of statistic, activity level, and frequency range, the probability distributions were calculated by binning the events between the same ranges in logarithmic bins for fair comparison. Below, the results for each frequency range are discussed in turn.

3.2.1. Low Frequency Chorus

The average survey and average peak burst powers for low frequency chorus are shown as a function of L^* and MLT for the three activity levels in Figures 10a–10c and 10e–10g, respectively. For all activities, the burst data set reproduces the spatial distribution of power found using the survey averages for low frequency chorus, even if there are differences in the absolute magnitude.

The power probability distributions within both Figures 10d and 10h demonstrate that low frequency chorus power has only a weak dependence on activity, with slightly heavier tails for moderate and active conditions. Additionally, there is a near-zero probability that the powers observed in the survey and burst will exceed the high-power threshold, shown by the black dashed horizontal line in each plot.

From the dial plots in Figures 10i–10k and 10m–10o, the metrics of variability, $P_{burst,max}/P_{survey}$ and IQR_{norm}, are both largest in the post-midnight sector for all activities. The probability distributions in Figures 10l and 10p show slightly heavier tails toward large variability for the active conditions.

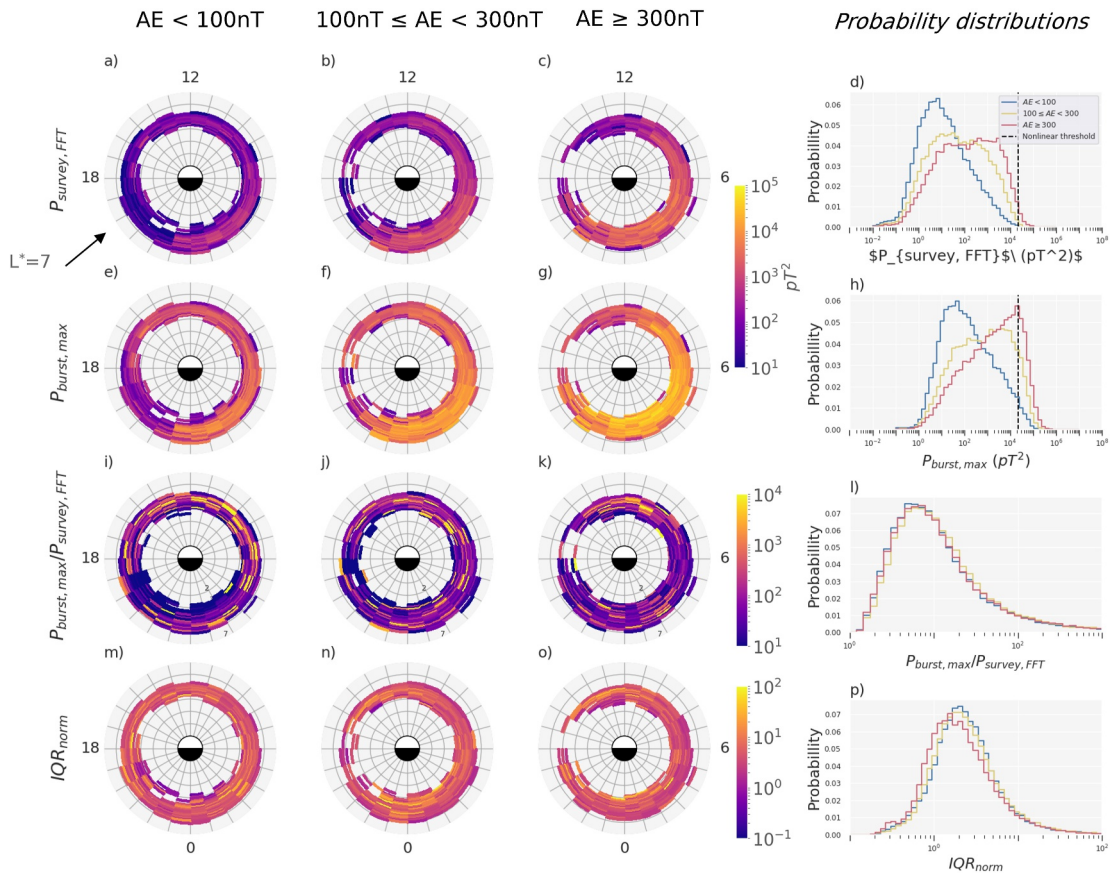

Figure 12. Upper-band chorus events at equatorial latitudes separated by activity into AE $<$ 100 nT, 100 nT $\leq$ AE $<$ 300 nT, and AE $\geq$ 300 nT. The sub-panels show the same statistics as before, with (a–c) average chorus power of survey events for which a burst record exists; (e–g) maximum chorus burst power; (i–k) ratio between the maximum chorus burst power and the survey power; and (m–o) $\frac{Q3-Q1}{Q2}$. Additionally, (d, h, l, p) show the probability distributions of survey power, peak power, power ratio, and the IQR_{norm} for these events, respectively. An estimate of a high-power threshold is given by the dashed red line on (d, h).

3.2.2. Lower-Band Chorus

The average survey lower-band chorus wave power increases with increasing activity, with an average intensity of 400 pT^2 during quiet times, up to 1×10^4 pT^2 during active times from 21:00 MLT through dawn to noon (Figures 11a–11c). The average lower-band chorus peak burst powers also increase with increasing activity, with an average power of 3×10^3 pT^2 during quiet times, moving up to 9×10^4 pT^2 during active times (Figures 11e–11g). Additionally, the peak burst powers showed the largest ratios relative to the survey power during active conditions. For instance, $P_{burst,max}/P_{survey} > 100$ in ∼9% of cases for AE $>$ 300 nT, decreasing to ∼6% and ∼3% of cases during moderate and quiet times, respectively.

The probability distributions of the survey and peak burst powers are shown in Figures 11d and 11h respectively. During active times a large fraction (∼25%) of the lower-band chorus peak burst power exceeds the high-power threshold. If we limit the MLT range to between 21:00–12:00 MLT, this percentage increases up to 46%. The survey powers can also exceed the high-power threshold, although these are less common, being seen in ∼8% of the observations. Furthermore, the peak burst power exhibits a double-peaked distribution during active times, with the second peak well in excess of the high-power threshold.

IQR_{norm}, shown in Figures 11m–11o, increases with increasing activity and is largest during active times in the region from 21:00 MLT through midnight to 10:00 MLT, largely corresponding to the region where the strongest waves are observed. This region and activity condition is also associated with the largest differences between the peak burst power and the average survey power, shown in Figure 11k. Furthermore, the probability distribution in

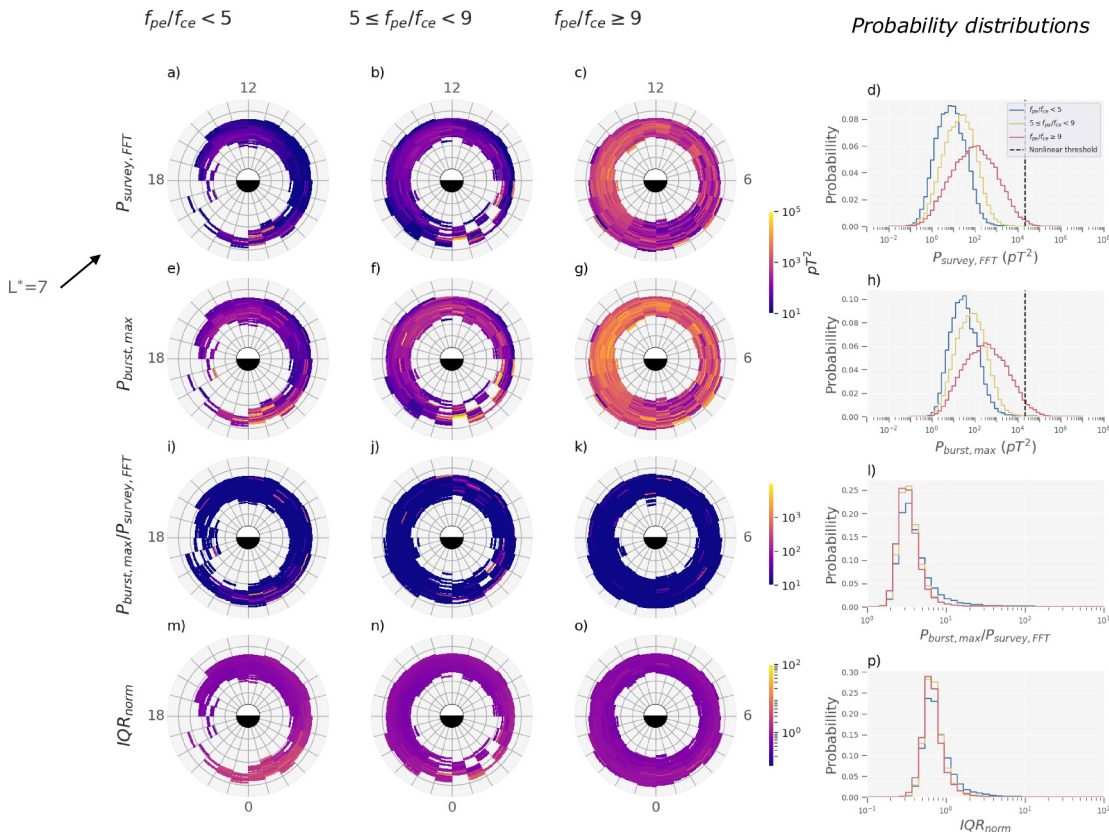

Figure 13. Low frequency chorus events at equatorial latitudes separated by f_{pe}/f_{ce} into $f_{pe}/f_{ce} < 5$, $5 \le f_{pe}/f_{ce} < 9$, and $f_{pe}/f_{ce} \ge 9$. The sub-panels show the same statistics as before, with (a–c) average chorus power of survey events for which a burst record exists; (e–g) maximum chorus burst power; (i–k) ratio between the maximum chorus burst power and the survey power; and (m–o) $\frac{Q3-Q1}{Q2}$. Additionally, (d, h, l, p) show the probability distributions of survey power, peak power, power ratio, and the IQR_{norm} for these events, respectively. An estimate of a high-power threshold is given by the dashed red line on (d, h).

Figure 11p reveals a secondary peak at higher values of IQR_{norm} during active times, with $IQR_{norm} > 1$ for ~54% of cases.

3.2.3. Upper-Band Chorus

The average upper-band chorus survey wave power increases with increasing activity, with an average intensity of 2×10^2 pT^2 during quiet times, up to 2×10^3 pT^2 during active times from 21:00 MLT through dawn to noon (Figures 12a–12c). Similarly, focused upon the same MLT sector, the upper-band chorus peak burst powers increase with increasing activity, with an average power of 2×10^3 pT^2 during quiet times, moving up to 1.6×10^4 pT^2 during active times (Figures 12e–12g).

Of the upper-band chorus waves identified during active times, ~18% have peak powers that exceed the high-power threshold. However, the survey powers rarely exceed the high-power threshold (Figures 12d and 12h).

However, in contrast to low frequency and lower-band chorus, the ratio of peak burst to survey power shown in Figures 12i–12k, is consistently large across all activity ranges and independent of MLT. Considering the probability distributions in Figure 12l, we find that $P_{burst,max}/P_{survey} > 100$ between ~7−8% of the time across all activities.

From Figures 12m–12o, and again in contrast to low frequency and lower-band chorus, IQR_{norm} is largely independent of MLT and activity. Furthermore, there are large differences in the shape of the probability distributions for IQR_{norm} between the lower- and upper-band waves. From Figure 11p, the distribution of IQR_{norm} for lower-band chorus is either a bimodal distribution (during active times), or a dominant single-peaked distribution at low values of IQR_{norm} followed by an extended tail at higher values (during quiet-moderate times). In

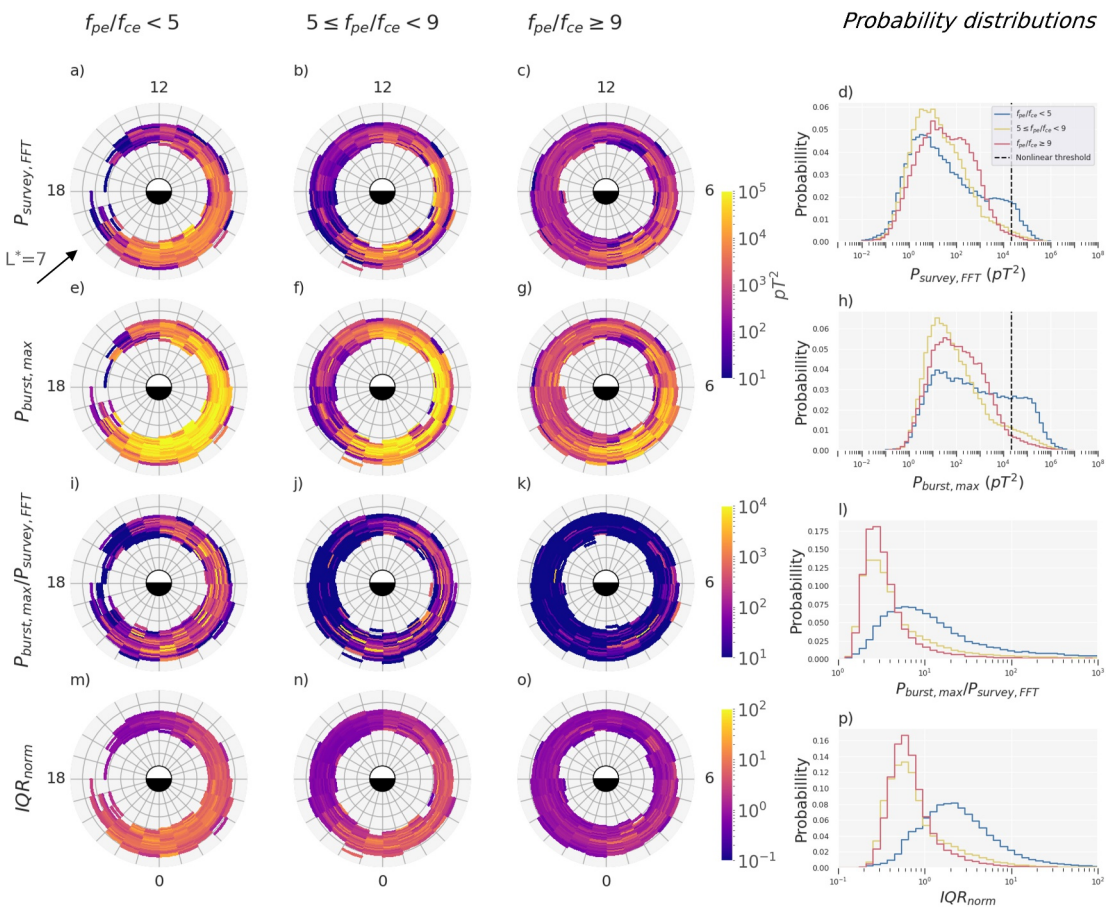

Figure 14. Lower-band chorus events at equatorial latitudes separated by f_{pe}/f_{ce} into $f_{pe}/f_{ce} < 5$, $5 \le f_{pe}/f_{ce} < 9$, and $f_{pe}/f_{ce} \ge 9$. The sub-panels show the same statistics as before, with (a–c) average chorus power of survey events for which a burst record exists; (e–g) maximum chorus burst power; (i–k) ratio between the maximum chorus burst power and the survey power; and (m–o) $\frac{Q3-Q1}{Q2}$. Additionally, (d, h, l, p) show the probability distributions of survey power, peak power, power ratio, and the IQR_{norm} for these events, respectively. An estimate of a high-power threshold is given by the dashed red line on (d, h).

comparison, across all activities, the distribution of IQR_{norm} in Figure 12p for upper-band chorus is a wide, single-peaked Gaussian, centered $\sim$2. This leads to an $IQR_{norm} > 1$ between $59 - 67\%$ of the time for upper-band chorus.

3.3. Dependence on f_{pe}/f_{ce}

The ratio of the electron plasma frequency to the electron gyrofrequency (f_{pe}/f_{ce}) is an important factor in determining the efficiency of wave particle interactions (Horne et al., 2003). Acceleration of electrons to relativistic energies is most efficient for lower-band chorus in regions of low f_{pe}/f_{ce} (Horne & Thorne, 2003; Meredith et al., 2002; Summers et al., 1998) and recent studies have demonstrated the importance of capturing the variability of the wave power and f_{pe}/f_{ce} in radiation belt modeling (e.g., Agapitov et al., 2019; Allison et al., 2021; Daggitt et al., 2024; Ross et al., 2021; Watt et al., 2019).

Furthermore, the value of f_{pe}/f_{ce} correlates with many spectral properties of chorus waves that can have implications in nonlinear theories, such as frequency band-width (Gao et al., 2014), chirping rate and time duration of subpackets (He et al., 2023).

The events were divided into three f_{pe}/f_{ce} groups; $f_{pe}/f_{ce} < 5$, $5 \le f_{pe}/f_{ce} < 9$, and $f_{pe}/f_{ce} \ge 9$. Binning by f_{pe}/f_{ce} resulted in 89 fewer chorus-containing samples owing to unavailable density measurements, corresponding to a small $\sim$0.01% reduction.

3.3.1. Low Frequency Chorus

Both survey and burst powers tend to increase with increasing f_{pe}/f_{ce} (Figures 13a–13c and 13e–13g, respectively). Furthermore, in each f_{pe}/f_{ce} range, the probability distributions of both powers are similar (Figures 13d and 13h). This suggests, similarly to the results shown in the previous section for activity, that the burst data set reproduces the spatial distribution of power found using the survey averages for low frequency chorus for all values of f_{pe}/f_{ce}, with the average maximum burst powers a factor of ∼3 larger than the average survey powers.

There are two significant features in the power distributions of low frequency waves, however, that become more evident following separation by f_{pe}/f_{ce}. First, there is a higher statistical likelihood of having larger powers at high f_{pe}/f_{ce}, evident in the probability distributions in Figures 13d and 13h, where the median power shifts by a factor of ∼100 for both the survey and burst powers when moving from low to high f_{pe}/f_{ce}. Additionally, these higher powers are focused on the afternoon sector. This afternoon feature was not observed when splitting the waves by AE, suggesting that this population exists across a range of activities.

Second, in contrast, there is a higher statistical likelihood of having large power variability at low f_{pe}/f_{ce} in the pre- and post-midnight sector, evident from large averages of both $P_{burst,max}/P_{survey}$ and IQR_{norm} (Figures 13i and 13m, respectively). For example, $P_{burst,max}/P_{survey}$ exceeds 10 for ∼10% of low f_{pe}/f_{ce} events, whilst this percentage dropped to ∼4% for events at medium-to-high f_{pe}/f_{ce}. Similarly, IQR_{norm} exceeds unity 17% of the time at low f_{pe}/f_{ce}, with this dropping again to ∼4% for events at medium-to-high f_{pe}/f_{ce}. Low frequency power in this MLT region did tend to increase with activity (Figures 10a–10c and 10e–10g), similar to the trends with activity observed for lower-band chorus.

3.3.2. Lower-Band Chorus

Globally, we again see the largest powers between 21:00, through midnight, onto 12:00 MLT for both the survey and peak burst powers across all f_{pe}/f_{ce} ranges (Figures 14a–14c and 14e–14g, respectively). Overall, however, the power shows a negative relationship with f_{pe}/f_{ce}. For instance, the average survey (peak burst) power in this post-midnight/dawn MLT region is $5.5 \times 10^3\ pT^2$ ($4.8 \times 10^4\ pT^2$) when f_{pe}/f_{ce} is low, decreasing to $1.5 \times 10^3\ pT^2$ ($9.0 \times 10^3\ pT^2$) when f_{pe}/f_{ce} is high. In other words, average powers for both survey and burst reduce by roughly a factor of ∼5 when moving from low to high f_{pe}/f_{ce}.

If we consider the fraction of lower-band waves that exceed the high-power threshold in each f_{pe}/f_{ce} range, we see that, in the peak burst powers, the threshold is exceeded ∼21.2% of the time at low f_{pe}/f_{ce}, with this proportion then falling to ∼6.7% and ∼3.4% at medium and high f_{pe}/f_{ce}, respectively. In comparison to the separation of lower-band waves by AE, parameterizing chorus wave power by f_{pe}/f_{ce} does not isolate the largest waves as distinctly.

For both $P_{burst,max}/P_{survey}$ and IQR_{norm}, the largest averages are again observed around post-midnight/dawn, but there is a negative correlation with f_{pe}/f_{ce} (Figures 14i–14k and 14m–14o, respectively). At low f_{pe}/f_{ce}, there is a ∼12.0% chance that $P_{burst,max}/P_{survey} > 100$, however this probability reduces to ∼3.9% and ∼1.2% for medium and high f_{pe}/f_{ce}, respectively. Finally, separating IQR_{norm} by f_{pe}/f_{ce} almost completely isolates the 'low' and 'high' variability peaks identified in the AE-separated probability distributions from Section 3.2.2. Consistent with this, we see a single peaked distribution with a mean IQR_{norm} of ∼2 at low f_{pe}/f_{ce}, whilst the mean IQR_{norm} for the medium and high f_{pe}/f_{ce} populations sits around 0.5.

3.3.3. Upper-Band Chorus

Similarly to lower-band, upper-band chorus wave power increases with decreasing f_{pe}/f_{ce} and is strongest from 21:00 MLT through midnight to 12:00 MLT. Within this MLT range, the average intensity is $\sim 1.4 \times 10^3\ pT^2$ ($\sim 1.2 \times 10^4\ pT^2$) when f_{pe}/f_{ce} is low, dropping to $\sim 4 \times 10^2\ pT^2$ ($\sim 3 \times 10^3\ T^2$) when f_{pe}/f_{ce} is high for survey power (peak burst power) (Figures 15a–15c and 15e–15g, respectively). From this, we can also say that the average peak burst powers are around a factor of 10 larger than the average survey powers within the region.

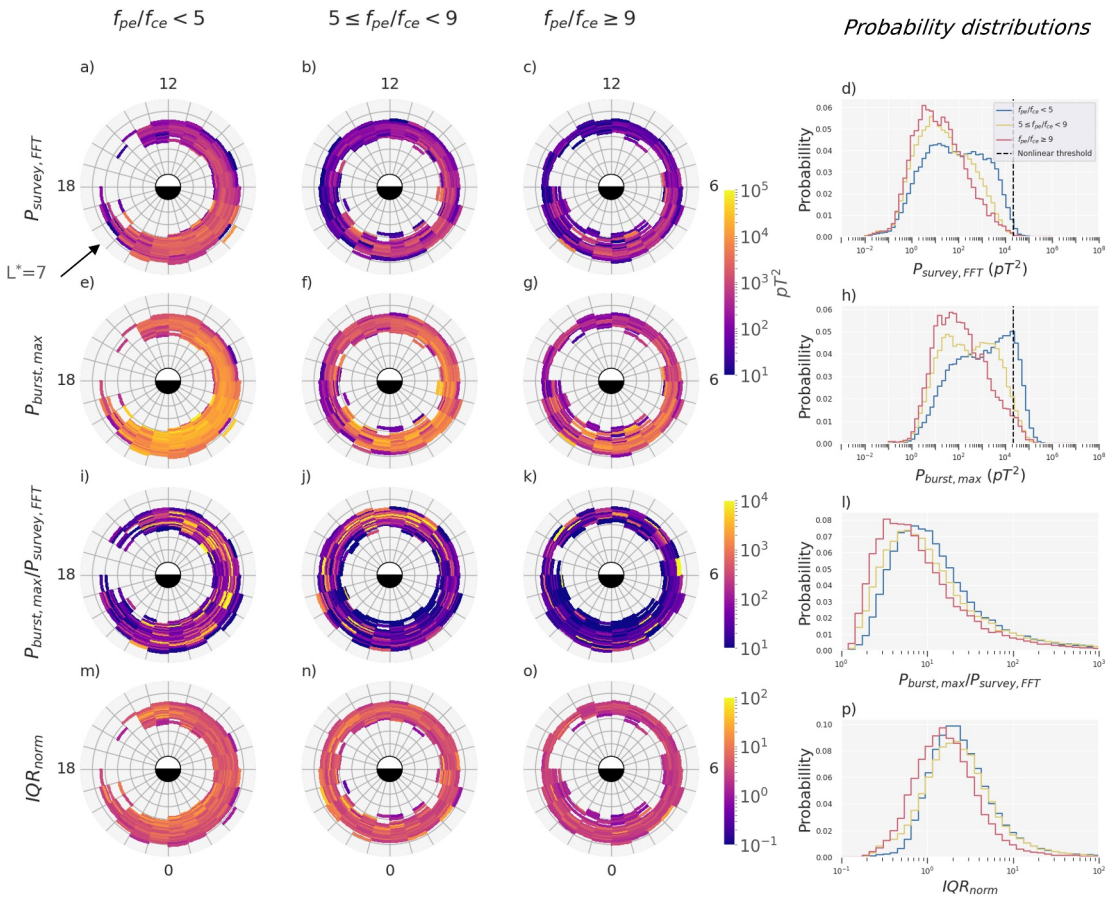

Figure 15. Upper-band chorus events at equatorial latitudes separated by f_{pe}/f_{ce} into $f_{pe}/f_{ce} < 5$, $5 \leq f_{pe}/f_{ce} < 9$, and $f_{pe}/f_{ce} \geq 9$. The sub-panels show the same statistics as before, with (a–c) average chorus power of survey events for which a burst record exists; (e–g) maximum chorus burst power; (i–k) ratio between the maximum chorus burst power and the survey power; and (m–o) $\frac{Q3-Q1}{Q2}$. Additionally, (d, h, l, p) show the probability distributions of survey power, peak power, power ratio, and the IQR_{norm} for these events, respectively. An estimate of a high-power threshold is given by the dashed red line on (d, h).

The average survey power rarely surpasses the high-power threshold. However, the peak burst power has a substantially higher probability of doing so, especially during low f_{pe}/f_{ce}, where there is a ∼14.5% chance that wave power will exceed the threshold, in comparison to ∼3−4% for both medium and high f_{pe}/f_{ce}.

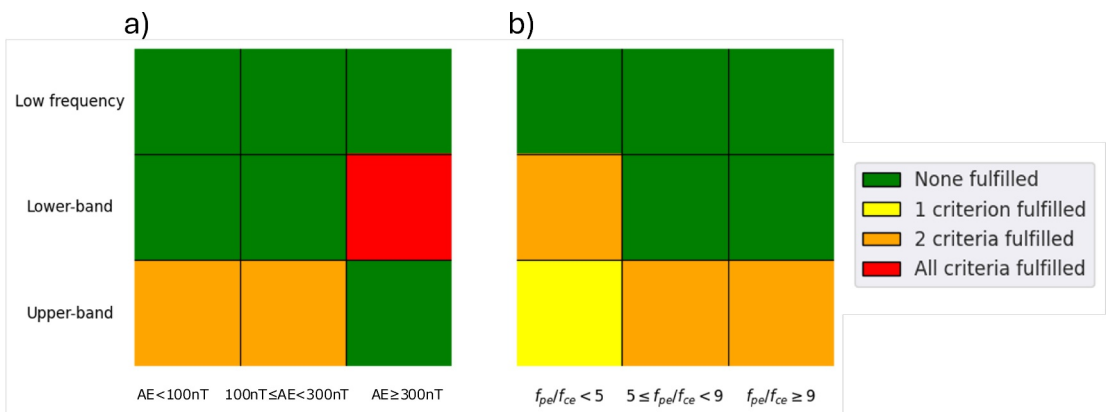

Figure 16. "Traffic light" rating of chorus wave sub-sets for low frequency, lower-band and upper-band chorus with all (a) AE ranges, and (b) f_{pe}/f_{ce} ranges.

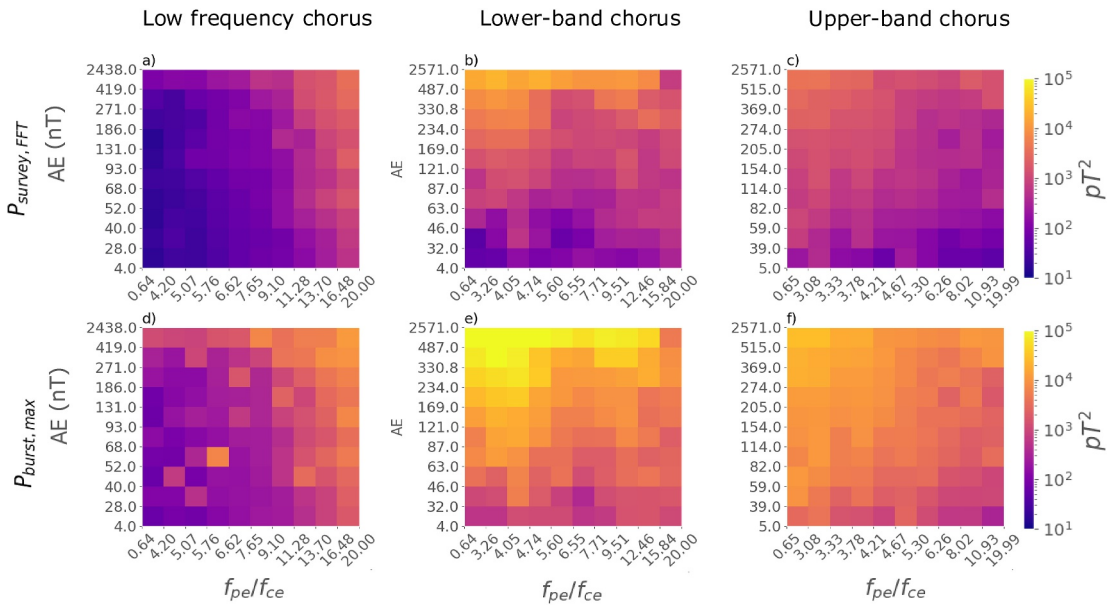

Figure 17. For low frequency, lower-band, and upper-band chorus, panels (a–c) show P_{survey} and panels (d–f) show $P_{burst,max}$ for the 10% quantile bins of $(AE, f_{pe}/f_{ce})$ at equatorial latitudes.

With the exception of having insufficient chorus events between 13:00 to 20:00 MLT for low f_{pe}/f_{ce}, the variability of upper-band chorus power is uniformly high across all MLTs, and shows a subtle decrease with increasing f_{pe}/f_{ce}. Notably, for all f_{pe}/f_{ce} ranges, the mean IQR_{norm} is $\sim$2 and there is a 5−9% chance that $P_{burst,max}/P_{survey} > 100$. This is almost identical to the behavior of these statistics with respect to AE in Section 3.2.3. This suggests that upper-band chorus power and its variability increase with decreasing f_{pe}/f_{ce}.

3.4. Comparison of Subset Power and Variability

In the previous sections, distributions of our four power metrics, P_{survey}, $P_{burst,max}$, $P_{burst,max}/P_{survey}$ ratio and IQR_{norm}, were presented for each combination of chorus frequency range and range of AE or f_{pe}/f_{ce}, respectively. There are two important features of the results for each combination that would be useful to compare; first, relative sub-second variability, and second, relative magnitude of the peak power on a sub-second scale.

First, to directly compare results for the sub-second variability, the distributions of $P_{burst,max}/P_{survey}$ ratio and IQR_{norm} in each subset of chorus, for example, lower-band chorus at low activity, were evaluated against the distributions for the complementary (remaining) population of all other chorus waves. More specifically, we estimate the statistically significant 75th percentile of each distribution using bootstrapping (Efron, 1979; Manly, 1997). This is a resampling method where, for each subset, we generated many new 'bootstrap' subsets by randomly sampling the original subset with replacement. This then gives a robust estimate of the distribution percentiles, with associated uncertainties. We describe the subset distribution as being significantly large if the bootstrapped estimate of the 75th percentile exceeded three times the bootstrapped 75th percentile of the complementary chorus population. This technique allows evaluation of which subset of chorus shows the largest differences from the global statistics, and therefore the largest sub-second variability. For further context, probability distributions of each statistic for the total population are provided in Figure S6 of Supporting Information S1. We also wish to reiterate that only samples within which chorus emissions were identified are considered in these distributions. This allows the physical relationships of each wave type with activity and f_{pe}/f_{ce} to be investigated without diluting the statistics.

Using a similar method, the relative magnitude of peak sub-second powers was assessed using the high-power threshold. If the peak burst power at the 75th percentile of a given subset distribution was larger than the high-power threshold, the subset in question was considered to be showing significant deviations from quasilinear requirements.

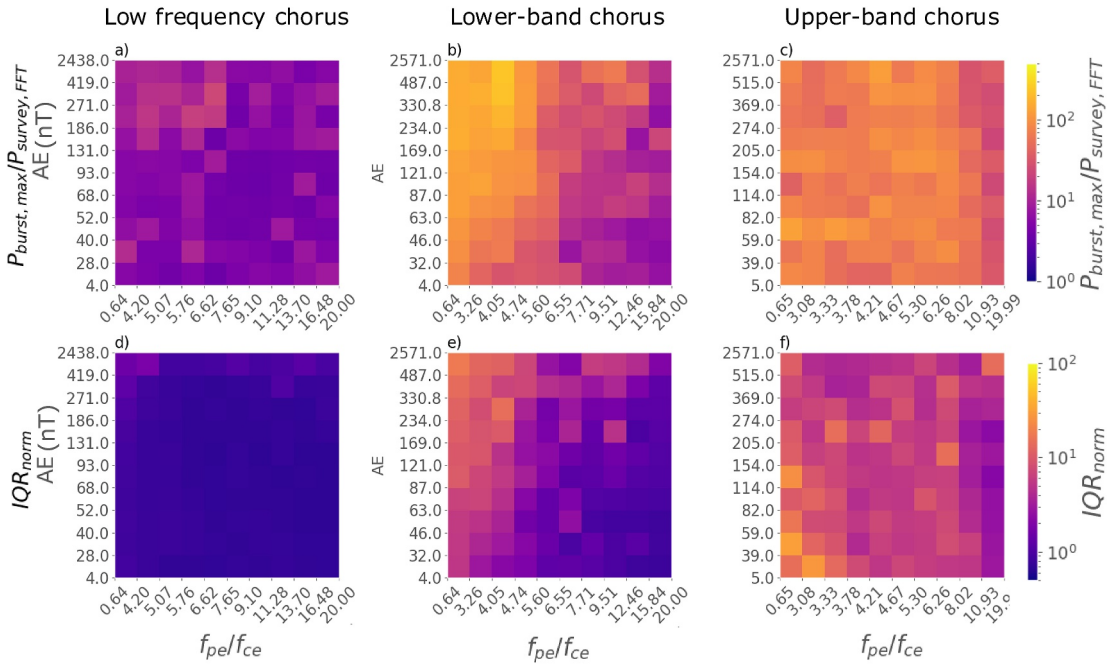

Figure 18. For low frequency, lower-band, and upper-band chorus, panels (a–c) show $P_{burst,max}/P_{survey}$ and panels (d–f) show IQR_{norm} for the 10% quantile bins of $(AE, f_{pe}/f_{ce})$ at off-equatorial latitudes.

Combining these criteria together, we have three thresholds:

1. $X_{0.75,subset} > 3X_{0.75,global}$, where $X = P_{burst,max}/P_{survey}$
2. $X_{0.75,subset} > 3X_{0.75,global}$, where $X = IQR_{norm}$
3. >25% of measurements exceed the approximate high-power threshold

Figure 16 illustrates a "traffic light" style rating of each chorus wave subset, split either by AE or f_{pe}/f_{ce}, where the number of the criteria fulfilled is given by the color; starting with green, indicating that no criteria are fulfilled, moving through yellow and amber, to all criteria fulfilled at red. Lower-band chorus waves at high activity were the only subset to fulfill all of the above criteria, suggesting that these waves show the largest deviations from the survey distributions, as well as being the most unsuitable for treatment by quasilinear theory.

3.5. Combined Dependence Upon AE and f_{pe}/f_{ce}

To further distinguish waves with low and high power variability, and thus identify which of AE index and the f_{pe}/f_{ce} ratio was potentially controlling the behavior, P_{survey}, $P_{burst,max}$, $P_{burst,max}/P_{survey}$ and IQR_{norm} were averaged in $(AE, f_{pe}/f_{ce})$ bins. The bins were determined by dividing the AE and f_{pe}/f_{ce} values, respectively, into 10% deciles such that there was roughly an equal number of observations in each bin. The resulting distributions are shown for the power in Figure 17, and for the variability in Figure 18. The distribution of AE and f_{pe}/f_{ce} values used to define the decile bins are provided in Figure S7 of Supporting Information S1.

The average survey power and average maximum burst power for each frequency band as a function of AE and f_{pe}/f_{ce} are shown in Figures 17a–17c and 17d–17f, respectively. There is a clear dependence of lower-band chorus power on activity, with higher AE leading to the largest power averages in both Figures 17b and 17e, and only a slight bias toward higher power at low f_{pe}/f_{ce} for each AE bin. Upper-band power shows a weaker dependence on both AE and f_{pe}/f_{ce}, while low frequency power averages are higher at high activity, and at large f_{pe}/f_{ce}.

If we then consider the results for $P_{burst,max}/P_{survey}$ and IQR_{norm} in Figure 18, the majority of high IQR_{norm} samples for lower-band chorus were observed during periods with low f_{pe}/f_{ce}. However, there was only a weak activity dependence as you move toward increasing AE in each f_{pe}/f_{ce} bin. This suggests that the ratio of plasma-to-gyrofrequency has a much larger impact on the variability of lower-band chorus wave power than the AE

activity index. Conversely, upper-band, shown in Figure 18f, displays a more uniform, large IQR_{norm} average across the entire (AE, f_{pe}/f_{ce}) space.

The combination of these results suggests that lower-band chorus power is well correlated with activity index, AE, but the normalized variability for these populations has a larger dependence upon f_{pe}/f_{ce}. Therefore, if we consider parameterizing by only activity or f_{pe}/f_{ce}, then we could be missing key distinguishing features in the lower-band populations.

4. Discussion

In our analysis, we identify features present in both the average $P_{burst,max}$ and P_{survey} power distributions that are consistent with current theories of chorus wave generation and propagation. First, at equatorial ($|\lambda_m| < 6°$) latitudes, close to the chorus source region (e.g., Burtis & Helliwell, 1976; Lauben et al., 2002; LeDocq et al., 1998), the distributions for lower-band chorus in Figures 8b and 8e, and for upper-band chorus in Figures 8c and 8f, had the largest survey and burst amplitudes in the post-midnight to dawn sector. Moderate lower-band power persisted into the dayside sector, but for a smaller range of L shells ($4 < L^* < 5$).

Second, as the waves propagate away from the equator ($|\lambda_m| \geq 6°$), they can experience damping due to the population of suprathermal electrons (Bortnik et al., 2007), and this damping is most efficient on the nightside for upper-band frequencies. In our observations, the lower-band intensity averages were shown to reduce from midnight to dawn in both distributions in Figures 9b and 9e. The upper-band chorus was hugely reduced in all (MLT, L^*) bins in both distributions shown in Figures 9c and 9f, supporting the suggestion that upper-band waves have been most efficiently damped. Finally, in both the low and high latitude distributions for low frequency chorus (Figures 8a, 8c, and 9a, 9c, respectively), the average $P_{burst,max}$ and P_{survey} were considerably lower than those observed for lower- and upper-band chorus, and peaked in the post-noon sector.

We observe two populations of low frequency chorus with different characteristics. One population peaks on the duskside, is strongest when f_{pe}/f_{ce} is large ($f_{pe}/f_{ce} > 9$) and is weakly dependent on AE. Furthermore, the duskside emissions are "hiss-like" in structure and associated with relatively low values of IQR_{norm} ($IQR_{norm} < 1$). These are similar in nature to the THEMIS observations of hiss-like emissions outside of the plasmasphere (Li et al., 2012). The location and nature of these emissions suggest that this population of low frequency chorus is a form of plasmaspheric hiss which has leaked out of the plasmasphere, known as exohiss (Seo & Kim, 2023; Wang et al., 2020; Watt et al., 2025; Zhu et al., 2019; Zou et al., 2024). The second population is strongest in the pre- and post-midnight sectors, is strongest during active conditions and when f_{pe}/f_{ce} is low. This subset of low frequency chorus wave is associated with larger values of IQR_{norm} ($IQR_{norm} > 3$). This population shows similar characteristics to lower- and upper-band chorus and is likely to be an extension of the lower-band chorus to lower frequencies.

In our work, the most intense lower-band chorus waves were observed during periods of high geomagnetic activity, and when $f_{pe}/f_{ce} < \sim 5$. Numerous past single-spacecraft studies (e.g., Li, Bortnik, et al., 2011; Meredith et al., 2001; Wang et al., 2019) and combined multi-spacecraft studies (e.g., Agapitov et al., 2018; Meredith et al., 2020) on 'survey-like' temporal resolutions have provided evidence that lower-band chorus waves are substorm-driven. Lower-band chorus occurrence and power has also been shown to correlate with low ratios of f_{pe}/f_{ce} (Li, Thorne, Nishimura, et al., 2010). We have additionally found that the maximum sub-second powers exhibit a larger average increase from quiet to active times, or when moving down from high to low f_{pe}/f_{ce}, compared to the survey power.

Whilst the likelihood of a nonlinear interaction is not solely dependent upon wave amplitude (e.g., Zhang et al., 2020), we see that >25% of the lower-band population surpassed the indicative high-power threshold during active times. Zhang et al. (2018) similarly observed, in both Van Allen Probes and THEMIS waveform measurements, that 'nonlinear' candidates for lower-band chorus were most prevalent in the midnight/dawn sectors under active conditions. Additionally, and with further analysis in Zhang et al. (2019), a large proportion of the intense waves they observed also had short packet durations (~10–20 wave periods). Unlike wave intensity, however, the packet duration did not show a dependence on AE. Whilst our study does not directly investigate wave packet duration, the magnitude of IQR_{norm} on a sub-second timescale can be closely associated with temporal variability across wave packets. Therefore, we also observed that whilst lower-band wave power

showed a positive correlation with AE, as demonstrated in Figure 17b, the temporal variability in Figure 18b showed very little dependence on AE.

If we instead consider the variability dependence upon f_{pe}/f_{ce}, the large values of IQR_{norm} were confined to regions of $f_{pe}/f_{ce} < 5$. This complements a study by He et al. (2023), in which the shortest, most rapidly changing and intense lower-band rising tone elements were observed at low values of f_{pe}/f_{ce}, using the EMFISIS burst data set. Furthermore, from THEMIS burst observations, Li et al. (2012) showed that discrete lower-band emissions were more likely to be seen under low f_{pe}/f_{ce} conditions, whilst "hiss-like" lower-band was more common under higher f_{pe}/f_{ce}.

The upper-band chorus power in $P_{burst,max}$ and P_{survey} was much lower on average than that observed for the lower-band chorus. However, it is also positively associated with AE, and has a slight preference for lower values of f_{pe}/f_{ce}, though both dependencies are weaker than those for lower-band chorus. On a sub-second timescale, we again saw a shift upwards in average $P_{burst,max}$ compared to P_{survey}, as well as a narrowing of the probability distribution at high activities. As shown in Sections 3.2, 3.3, and 3.5, the $P_{burst,max}/P_{survey}$ and IQR_{norm} had almost no dependence upon activity or f_{pe}/f_{ce}. However, the distributions peaked at large values in all cases in comparison to the low frequency and lower-band chorus. This suggests that, whilst upper-band has lower average powers, the underlying wave structure may be more similar to the 'discrete," highly variable population of lower-band waves.

The spatiotemporal variability of plasma waves on various time and length scales, and the impact upon quasi-linear diffusion coefficient calculations have been considered in other studies. Using Van Allen Probes wave measurements averaged over 5-min timescales, Watt et al. (2025) identified two distinct populations of chorus, distinguishable by low and high power variability. The low variability population was observed primarily on the day-side, within $f_{LHR} < f < 0.1f_{ce}$, and had little dependence upon AE. This population is in the same frequency and MLT range as the low variability, low frequency emissions presented in this paper. This suggests that low frequency chorus waves have repeating trends in variability across the sub-second to 5-min timescales. The high variability population focused upon in Watt et al. (2025) was observed on the night-side, between 00:00–08:00 MLT in the lower- and upper-band frequency ranges. This population had a positive relationship with AE, with a similar response to our observations for lower- and upper-band chorus. In Watt et al. (2017), using Cluster measurements over many years, it was shown that distributions of whistler-mode wave power binned by activity were not Gaussian and therefore the mean value was a poor representation of the underlying variability. Such variability around statistical averages of wave properties has been investigated for other wave modes, such as EMIC waves (e.g., Ross et al., 2020), lightning generated whistlers (e.g., Shane et al., 2025), and hiss waves (e.g., Zhang et al., 2021).

It has been shown that the acceleration of MeV electrons due to interactions with chorus waves is sensitive to changes in f_{pe}/f_{ce}, particularly when there are decreases in f_{pe}/f_{ce} during active periods (Agapitov et al., 2019). Assuming we consider only quasi-parallel waves, the latitude corresponding to resonance with MeV electrons becomes smaller with decreasing f_{pe}/f_{ce}. In Section 3.5, we showed that lower-band chorus waves had the largest average power and sub-second variability at low f_{pe}/f_{ce} (<5) during active conditions (AE > 300 nT), and at equatorial latitudes. Future work could build on these results to further constrain the timescales of electron acceleration and loss due to interactions with chorus waves with respect to f_{pe}/f_{ce} and activity, informed by the higher-resolution burst-mode wave data that we show. Interestingly, we note that multiple studies show that average plasmaspheric hiss power on the dayside tends to increase with geomagnetic activity (e.g., Meredith et al., 2004; N. Liu et al., 2020; Su et al., 2018), with Agapitov et al. (2020) finding that f_{pe}/f_{ce} decreases in the plasmasphere during active periods (AE > 150 nT) and results in shorter MeV electron lifetimes.

Whilst we have investigated the power variability of low frequency, lower- and upper-band chorus, respectively, the variability of the underlying spectra on finer frequency resolution has not been considered. However, the spectra of chorus wave power is key in accurately determining the energy of the electrons most likely to interact with the waves. Future work could therefore focus on power spectra variability, and using numerical experiments to assess the potential implications of sub-second variability upon quasilinear diffusion coefficient calculations.

5. Conclusions

In this study we analyze 7 years of EMFISIS wave data from Van Allen Probes A and B to investigate the behavior of the chorus wave power on sub-second timescales. We note that the average values quoted below were calculated in the presence of chorus waves identified in the survey data in the appropriate band, and only when a corresponding burst sample existed (~5% of all chorus-containing survey samples). Therefore, our study provides a full statistical analysis of direct 1-to-1 comparisons between simultaneous and co-located burst- and survey-mode measurements. Lower-band and low frequency waves were identified in ~78% of all chorus-containing burst samples, whilst upper-band was identified in ~22%. Our principle findings are:

1. Low frequency chorus in the region 11:00–22:00 MLT was strongest when f_{pe}/f_{ce} was large ($f_{pe}/f_{ce} > 9$) with average survey and peak burst powers of 1.3×10^3 and $4.5 \times 10^3 pT^2$ respectively and showed low variability ($IQR_{norm} < 1$), consistent with exohiss.
2. Low frequency chorus near midnight (22:00–04:00 MLT) was strongest during active conditions when f_{pe}/f_{ce} was low ($f_{pe}/f_{ce} < 5$) with average survey and peak burst powers of 1.5×10^2 and 1.3×10^3 pT^2 respectively and showed high variability ($IQR_{norm} > 3$), consistent with the chorus emissions at higher relative frequencies.
3. Lower-band chorus was strongest near the equator in the region 21:00–12:00 MLT during active conditions across the entire observed range of f_{pe}/f_{ce}, with average survey and peak burst powers of 1×10^4 and 9×10^4 pT^2 respectively.
4. Lower-band chorus waves also showed significant variability ($IQR_{norm} \sim 3$) in the region 21:00–12:00 MLT, primarily during active conditions and/or low values of f_{pe}/f_{ce} ($f_{pe}/f_{ce} < 5$).
5. During active conditions, the average survey wave power exceeded the high-power threshold in ~8% of the observations of lower-band chorus. However, on sub-second "burst" timescales, over 25% of the observations exceeded the high-power threshold, with this percentage increasing to 46% when only considering the 21:00–12:00 MLT range.
6. Upper-band chorus was strongest near the equator in the region 21:00–12:00 MLT during active conditions and/or low f_{pe}/f_{ce} ($f_{pe}/f_{ce} < 5$), with average survey and peak burst powers of $\sim 2 \times 10^3$ and $\sim 1.5 \times 10^4$ pT^2 respectively.
7. Upper-band chorus waves showed high variability ($IQR_{norm} > 2$) across all local times for all activities and values of f_{pe}/f_{ce}.
8. The average survey upper-band chorus wave power rarely exceeded the high-power threshold. In contrast, on sub-second "burst" timescales, ~15% of the observations exceeded the high-power threshold.

Finally, by assessing the implications of sub-second power and variability together, we found that lower-band chorus at high AE will deviate most significantly from averaged spacecraft "surveys," as well as from requirements of quasilinear theory. It is clear, however, that whilst upper-band chorus waves are weaker emissions than those in the lower-band, on a sub-second timescale they consistently display significant differences to the averaged 'survey' spectra. These results motivate further investigation into how sub-second variability of chorus wave power in different frequency bands may affect calculation of diffusion coefficients in quasilinear modeling.

Conflict of Interest

The authors declare no conflicts of interest relevant to this study.

Availability Statement

All data used for this analysis is freely available. The Van Allen Probes EMFISIS data may be obtained from http://emfisis.physics.uiowa.edu/data/index, and the activity indices are available from Omniweb at https://omniweb.gsfc.nasa.gov/.

Acknowledgments
The authors acknowledge the Van Allen Probes project team for EMFISIS data at https://emfisis.physics.uiowa.edu/data/index, and the Omniweb project team for the provision of AE index data at https://omniweb.gsfc.nasa.gov/. RB would like to acknowledge support from the University of Exeter, the British Antarctic Survey and the United Kingdom Research and Innovation (UKRI) Natural Environment Research Council (NERC) GW4+ DTP2 NE/S007504/1 studentship project 2697077. OA would like to acknowledge support from the University of Birmingham, and also from the UKRI NERC Independent Research Fellowship NE/V013963/1 and NE/V013963/2. NM would like to acknowledge funding from the NERC Grants NE/V00249X/1 (SatRisk), NE/X000389/1 and NE/R016038/1. DPH acknowledges support from the National Aeronautics and Space Administration under Grants 80NSSC20K1324 and 80NSSC21K0519, in addition to support from the National Science Foundation Geospace Environment Modeling program under Grant 2350235. AH would like to acknowledge support from STFC Research Grants ST/R000891/1, ST/V000659/1 and No. ST/Y00230X/1. This research was supported by the International Space Science Institute (ISSI) in Bern, through ISSI International Team project 'Beyond Diffusion: Advancing Earth's Radiation Belt Models with Nonlinear Dynamics' (ISSI Team project #25–640). For the purpose of open access, the author has applied a Creative Commons Attribution (CC BY) licence to any Author Accepted Manuscript version arising from this submission.

References

Agapitov, O., Mourenas, D., Artemyev, A., Claudepierre, S. G., Hospodarsky, G., & Bonnell, J. W. (2020). Lifetimes of relativistic electrons as determined from plasmaspheric hiss scattering rates statistics: Effects of ω_{pe}/Ω_{ce} and wave frequency dependence on geomagnetic activity. *Geophysical Research Letters*, *47*(13), e2020GL088052. https://doi.org/10.1029/2020GL088052

Agapitov, O., Mourenas, D., Artemyev, A., Hospodarsky, G., & Bonnell, J. (2019). Time scales for electron quasi-linear diffusion by lower-band chorus waves: The effects of ω_{pe}/Ω_{ce} dependence on geomagnetic activity. *Geophysical Research Letters*, *46*(12), 6178–6187. https://doi.org/10.1029/2019GL083446

Agapitov, O. V., Artemyev, A. V., Mourenas, D., Krasnoselskikh, V., Bonnell, J., Contel, O. L., et al. (2014). The quasi-electrostatic mode of chorus waves and electron nonlinear acceleration. *Journal of Geophysical Research: Space Physics*, *119*(3), 1606–1626. https://doi.org/10.1002/2013JA019223

Agapitov, O. V., Artemyev, A. V., Mourenas, D., Mozer, F. S., & Krasnoselskikh, V. (2015). Empirical model of lower band chorus wave distribution in the outer radiation belt. *Journal of Geophysical Research: Space Physics*, *120*(12), 10425–10442. https://doi.org/10.1002/2015JA021829

Agapitov, O. V., Mourenas, D., Artemyev, A. V., Mozer, F. S., Hospodarsky, G., Bonnell, J., & Krasnoselskikh, V. (2018). Synthetic empirical chorus wave model from combined van Allen probes and cluster statistics. *Journal of Geophysical Research: Space Physics*, *123*(1), 297–314. https://doi.org/10.1002/2017JA024843

Albert, J. M., Meredith, N. P., & Horne, R. B. (2009). Three-dimensional diffusion simulation of outer radiation belt electrons during the 9 October 1990 magnetic storm. *Journal of Geophysical Research*, *114*(A9). https://doi.org/10.1029/2009JA014336

Allanson, O., Ma, D., Osmane, A., Albert, J. M., Bortnik, J., Watt, C. E. J., et al. (2024). The challenge to understand the zoo of particle transport regimes during resonant wave-particle interactions for given survey-mode wave spectra. *Frontiers in Astronomy and Space Sciences*, *11*, 1332931. https://doi.org/10.3389/fspas.2024.1332931

Allison, H. J., Shprits, Y. Y., Zhelavskaya, I. S., Wang, D., & Smirnov, A. G. (2021). Gyroresonant wave-particle interactions with chorus waves during extreme depletions of plasma density in the Van Allen radiation belts. *Science Advances*, *7*(5), eabc0380. https://doi.org/10.1126/sciadv.abc0380

Artemyev, A. V., Mourenas, D., Zhang, X.-J., Agapitov, O., Neishtadt, A. I., Vainchtein, D. L., et al. (2025). Nonlinear resonant interactions of radiation belt electrons with intense whistler-mode waves. *Space Science Reviews*, *221*(1), 18. https://doi.org/10.1007/s11214-025-01144-y

Artemyev, A. V., Mourenas, D., Zhang, X.-J., & Vainchtein, D. (2022). On the incorporation of nonlinear resonant wave-particle interactions into radiation belt models. *Journal of Geophysical Research: Space Physics*, *127*(9), e2022JA030853. https://doi.org/10.1029/2022JA030853

Aryan, H., Agapitov, O. V., Artemyev, A., Mourenas, D., Balikhin, M. A., Boynton, R., & Bortnik, J. (2020). Outer radiation belt electron lifetime model based on combined Van Allen probes and cluster VLF measurements. *Journal of Geophysical Research: Space Physics*, *125*(8), e2020JA028018. https://doi.org/10.1029/2020JA028018

Aryan, H., Bortnik, J., Meredith, N. P., Horne, R. B., Sibeck, D. G., & Balikhin, M. A. (2021). Multi-parameter chorus and plasmaspheric hiss wave models. *Journal of Geophysical Research: Space Physics*, *126*(1), e2020JA028403. https://doi.org/10.1029/2020JA028403

Aryan, H., Yearby, K., Balikhin, M., Agapitov, O., Krasnoselskikh, V., & Boynton, R. (2014). Statistical study of chorus wave distributions in the inner magnetosphere using ae and solar wind parameters. *Journal of Geophysical Research: Space Physics*, *119*(8), 6131–6144. https://doi.org/10.1002/2014JA019939

Bingham, S. T., Mouikis, C. G., Kistler, L. M., Boyd, A. J., Paulson, K., Farrugia, C. J., et al. (2018). The outer radiation belt response to the storm time development of seed electrons and chorus wave activity during CME and CIR driven storms. *Journal of Geophysical Research: Space Physics*, *123*(12), 10139–10157. https://doi.org/10.1029/2018JA025963

Bortnik, J., Thorne, R. M., & Inan, U. S. (2008). Nonlinear interaction of energetic electrons with large amplitude chorus. *Geophysical Research Letters*, *35*(21). https://doi.org/10.1029/2008GL035500

Bortnik, J., Thorne, R. M., & Meredith, N. P. (2007). Modeling the propagation characteristics of chorus using CRRES suprathermal electron fluxes. *Journal of Geophysical Research*, *112*(A8). https://doi.org/10.1029/2006JA012237

Burtis, W. J., & Helliwell, R. A. (1969). Banded chorus—a new type of VLF radiation observed in the magnetosphere by OGO 1 and OGO 3. *Journal of Geophysical Research (1896-1977)*, *74*(11), 3002–3010. https://doi.org/10.1029/JA074i011p03002

Burtis, W. J., & Helliwell, R. A. (1976). Magnetospheric chorus: Occurrence patterns and normalized frequency. *Planetary and Space Science*.

Carpenter, D. L. (1963). Whistler evidence of a "knee" in the magnetospheric ionization density profile. *Journal of Geophysical Research (1896-1977)*, *68*(6), 1675–1682. https://doi.org/10.1029/JZ068i006p01675

Carpenter, D. L. (1966). Whistler studies of the plasmapause in the magnetosphere: 1. temporal variations in the position of the knee and some evidence on plasma motions near the knee. *Journal of Geophysical Research (1896-1977)*, *71*(3), 693–709. https://doi.org/10.1029/JZ071i003p00693

Cattell, C., Wygant, J. R., Goetz, K., Kersten, K., Kellogg, P. J., von Rosenvinge, T., et al. (2008). Discovery of very large amplitude whistler-mode waves in Earth's radiation belts. *Geophysical Research Letters*, *35*(1). https://doi.org/10.1029/2007GL032009

Chakraborty, S., Mann, I. R., Olifer, L., Black, R., Allanson, O., Rae, I. J., et al. (2025). Diagnosing the rapid loss of outer radiation belt electrons due to strong chorus-driven wave-particle interactions along an electron injection path. *Journal of Geophysical Research: Space Physics*, *130*(8), e2025JA034045. https://doi.org/10.1029/2025JA034045

Cully, C. M., Bonnell, J. W., & Ergun, R. E. (2008). Themis observations of long-lived regions of large-amplitude whistler waves in the inner magnetosphere. *Geophysical Research Letters*, *35*(17). https://doi.org/10.1029/2008GL033643

Daggitt, T., Horne, R., Glauert, S., Del Zanna, G., & Albert, J. M. (2024). Chorus wave power at the strong diffusion limit overcomes electron losses due to strong diffusion. *Nature Communications*, *15*(1800), 1800. https://doi.org/10.1038/s41467-024-45967-9

Drozdov, A. Y., Shprits, Y. Y., Orlova, K. G., Kellerman, A. C., Subbotin, D. A., Baker, D. N., et al. (2015). Energetic, relativistic, and ultra-relativistic electrons: Comparison of long-term verb code simulations with Van Allen Probes measurements. *Journal of Geophysical Research: Space Physics*, *120*(5), 3574–3587. https://doi.org/10.1002/2014JA020637

Efron, B. (1979). Bootstrap methods: Another look at the jackknife. *Annals of Statistics*, *7*(1), 1–26. https://doi.org/10.1214/aos/1176344552

Fok, M.-C., Horne, R. B., Meredith, N. P., & Glauert, S. A. (2008). Radiation belt environment model: Application to space weather nowcasting. *Journal of Geophysical Research*, *113*(A3). https://doi.org/10.1029/2007JA012558

Foster, J. C., Erickson, P. J., Omura, Y., Baker, D. N., Kletzing, C. A., & Claudepierre, S. G. (2017). Van Allen Probes observations of prompt MEV radiation belt electron acceleration in nonlinear interactions with VLF chorus. *Journal of Geophysical Research: Space Physics*, *122*(1), 324–339. https://doi.org/10.1002/2016JA023429

Gao, X., Li, W., Thorne, R. M., Bortnik, J., Angelopoulos, V., Lu, Q., et al. (2014). Statistical results describing the bandwidth and coherence coefficient of whistler mode waves using THEMIS waveform data. *Journal of Geophysical Research: Space Physics*, *119*(11), 8992–9003. https://doi.org/10.1002/2014JA020158

Gao, X., Lu, Q., Bortnik, J., Li, W., Chen, L., & Wang, S. (2016). Generation of multiband chorus by lower band cascade in the Earth's magnetosphere. *Geophysical Research Letters*, *43*(6), 2343–2350. https://doi.org/10.1002/2016GL068313

Glauert, S. A., & Horne, R. B. (2005). Calculation of pitch angle and energy diffusion coefficients with the Padie code. *Journal of Geophysical Research*, *110*(A4). https://doi.org/10.1029/2004JA010851

Glauert, S. A., Horne, R. B., & Meredith, N. P. (2014). Three-dimensional electron radiation belt simulations using the bas radiation belt model with new diffusion models for chorus, plasmaspheric HISS, and lightning-generated whistlers. *Journal of Geophysical Research: Space Physics*, *119*(1), 268–289. https://doi.org/10.1002/2013JA019281

Hartley, D. P., Christopher, I. W., Kletzing, C. A., Kurth, W. S., Santolik, O., Kolmasova, I., et al. (2023). Chorus wave properties from Van Allen Probes: Quantifying the impact of the sheath corrected electric field. *Geophysical Research Letters*, *50*(7), e2023GL102922. https://doi.org/10.1029/2023GL102922

Hartley, D. P., Kletzing, C. A., Chen, L., Horne, R. B., & Santolík, O. (2019). Van Allen Probes observations of chorus wave vector orientations: Implications for the chorus-to-HISS mechanism. *Geophysical Research Letters*, *46*(5), 2337–2346. https://doi.org/10.1029/2019GL082111

Hartley, D. P., Kletzing, C. A., Santolík, O., Chen, L., & Horne, R. B. (2018). Statistical properties of plasmaspheric hiss from Van Allen Probes observations. *Journal of Geophysical Research: Space Physics*, *123*(4), 2605–2619. https://doi.org/10.1002/2017JA024593

He, J., Xia, Z., & Chen, L. (2023). Statistical properties of lower band rising tone chorus waves. *Journal of Geophysical Research: Space Physics*, *128*(9), e2023JA031528. https://doi.org/10.1029/2023JA031528

Horne, R. B., Glauert, S. A., & Thorne, R. M. (2003). Resonant diffusion of radiation belt electrons by whistler-mode chorus. *Geophysical Research Letters*, *30*(9). https://doi.org/10.1029/2003GL016963

Horne, R. B., Thorne, R., Shprits, Y., Meredith, N. P., Glauert, S. A., Smith, A. J., et al. (2005). Wave acceleration of electrons in the Van Allen radiation belts. *Nature*, *437*(7056), 227–230. https://doi.org/10.1038/nature03939

Horne, R. B., & Thorne, R. M. (2003). Relativistic electron acceleration and precipitation during resonant interactions with whistler-mode chorus. *Geophysical Research Letters*, *30*(10). https://doi.org/10.1029/2003GL016973

Jaynes, A. N., Baker, D. N., Singer, H. J., Rodriguez, J. V., Loto'aniu, T. M., Ali, A. F., et al. (2015). Source and seed populations for relativistic electrons: Their roles in radiation belt changes. *Journal of Geophysical Research: Space Physics*, *120*(9), 7240–7254. https://doi.org/10.1002/2015JA021234

Karpman, V. (1974). Nonlinear effects in the elf waves propagating along the magnetic field in the magnetosphere. *Space Science Reviews*, *16*(3), 361–388. https://doi.org/10.1007/BF00171564

Kellogg, P. J., Cattell, C. A., Goetz, K., Monson, S. J., & Wilson III, L. B. (2010). Electron trapping and charge transport by large amplitude whistlers. *Geophysical Research Letters*, *37*(20). https://doi.org/10.1029/2010GL044845

Kennel, C. F., & Engelmann, F. (1966). Velocity space diffusion from weak plasma turbulence in a magnetic field. *Physics of Fluids*, *9*(2377), 2377–2388. https://doi.org/10.1063/1.1761629

Kennel, C. F., & Petschek, H. E. (1966). Limit on stably trapped particle fluxes. *Journal of Geophysical Research (1896-1977)*, *71*(1), 1–28. https://doi.org/10.1029/JZ071i001p00001

Kletzing, C., Bortnik, J., Hospodarsky, G., Kurth, W., Santolik, O., Smitth, C., et al. (2023). The electric and magnetic fields instrument suite and integrated science (EMFISIS): Science, data, and usage best practices. *Space Science Reviews*, *219*(4), 28. https://doi.org/10.1007/s11214-023-00973-z

Kletzing, C., Kurth, W., Acuna, M., MacDowall, R., Torbert, R., & Averkamp, T. (2013). The electric and magnetic field instrument suite and integrated science (EMFISIS) on RBSP. *Space Science Reviews*, *179*, 127–181.

Koskinen, H. E., & Kilpua, E. K. (2022). *Physics of earth's radiation belts: Theory and observations*. Springer Nature.

Kurita, S., Miyoshi, Y., Kasahara, S., Yokota, S., Kasahara, Y., Matsuda, S., et al. (2018). Deformation of electron pitch angle distributions caused by upper band chorus observed by the Arase satellite. *Geophysical Research Letters*, *45*(16), 7996–8004. https://doi.org/10.1029/2018GL079104

Kurth, W. S., De Pascuale, S., Faden, J. B., Kletzing, C. A., Hospodarsky, G. B., Thaller, S., & Wygant, J. R. (2015). Electron densities inferred from plasma wave spectra obtained by the waves instrument on Van Allen Probes. *Journal of Geophysical Research: Space Physics*, *120*(2), 904–914. https://doi.org/10.1002/2014JA020857

Lauben, D. S., Inan, U. S., Bell, T. F., & Gurnett, D. A. (2002). Source characteristics of ELF/VLF chorus. *Journal of Geophysical Research*, *107*(A12), SMP10-1–17. https://doi.org/10.1029/2000JA003019

LeDocq, M. J., Gurnett, D. A., & Hospodarsky, G. B. (1998). Chorus source locations from VLF poynting flux measurements with the polar spacecraft. *Geophysical Research Letters*, *25*(21), 4063–4066. https://doi.org/10.1029/1998GL900071

Li, W., Bortnik, J., Thorne, R. M., & Angelopoulos, V. (2011). Global distribution of wave amplitudes and wave normal angles of chorus waves using THEMIS wave observations. *Journal of Geophysical Research*, *116*(A12). https://doi.org/10.1029/2011JA017035

Li, W., Mourenas, D., Artemyev, A. V., Agapitov, O. V., Bortnik, J., Albert, J. M., et al. (2014). Evidence of stronger pitch angle scattering loss caused by oblique whistler-mode waves as compared with quasi-parallel waves. *Geophysical Research Letters*, *41*(17), 6063–6070. https://doi.org/10.1002/2014GL061260

Li, W., Santolik, O., Bortnik, J., Thorne, R. M., Kletzing, C. A., Kurth, W. S., & Hospodarsky, G. B. (2016). New chorus wave properties near the equator from Van Allen Probes wave observations. *Geophysical Research Letters*, *43*(10), 4725–4735. https://doi.org/10.1002/2016GL068780

Li, W., Thorne, R. M., Bortnik, J., Nishimura, Y., Angelopoulos, V., Chen, L., et al. (2010). Global distributions of suprathermal electrons observed on THEMIS and potential mechanisms for access into the plasmasphere. *Journal of Geophysical Research*, *115*(A12). https://doi.org/10.1029/2010JA015687

Li, W., Thorne, R. M., Bortnik, J., Shprits, Y. Y., Nishimura, Y., Angelopoulos, V., et al. (2011). Typical properties of rising and falling tone chorus waves. *Geophysical Research Letters*, *38*(14). https://doi.org/10.1029/2011GL047925

Li, W., Thorne, R. M., Bortnik, J., Tao, X., & Angelopoulos, V. (2012). Characteristics of HISS-like and discrete whistler-mode emissions. *Geophysical Research Letters*, *39*(18). https://doi.org/10.1029/2012GL053206

Li, W., Thorne, R. M., Nishimura, Y., Bortnik, J., Angelopoulos, V., McFadden, J. P., et al. (2010). Themis analysis of observed equatorial electron distributions responsible for the chorus excitation. *Journal of Geophysical Research*, *115*(A6). https://doi.org/10.1029/2009JA014845

Liu, N., Su, Z., Gao, Z., Zheng, H., Wang, Y., Wang, S., et al. (2020). Comprehensive observations of substorm-enhanced plasmaspheric HISS generation, propagation, and dissipation. *Geophysical Research Letters*, *47*(2), e2019GL086040. https://doi.org/10.1029/2019GL086040

Liu, X., Chen, L., & Xia, Z. (2020). The relation between electron cyclotron harmonic waves and plasmapause: Case and statistical studies. *Geophysical Research Letters*, *47*(9), e2020GL087365. https://doi.org/10.1029/2020GL087365

Lohmeyer, W., Carlton, A., Wong, F., Bodeau, M., Kennedy, A., & Cahoy, K. (2015). Response of geostationary communications satellite solid-state power amplifiers to high-energy electron fluence. *Space Weather*, *13*(5), 298–315. https://doi.org/10.1002/2014SW001147

Lyons, L. R. (1974). Pitch angle and energy diffusion coefficients from resonant interactions with ion–cyclotron and whistler waves. *Journal of Plasma Physics*, *12*(3), 417–432. https://doi.org/10.1017/S002237780002537X

Lyons, L. R., Thorne, R. M., & Kennel, C. F. (1972). Pitch-angle diffusion of radiation belt electrons within the plasmasphere. *Journal of Geophysical Research (1896-1977)*, *77*(19), 3455–3474. https://doi.org/10.1029/JA077i019p03455

Malaspina, D. M., Jaynes, A. N., Hospodarsky, G., Bortnik, J., Ergun, R. E., & Wygant, J. (2017). Statistical properties of low-frequency plasmaspheric hiss. *Journal of Geophysical Research: Space Physics*, *122*(8), 8340–8352. https://doi.org/10.1002/2017JA024328

Manly, B. F. J. (1997). *Randomization, bootstrap, and Monte Carlo methods in biology*. Chapman Hall.

Mauk, B., Fox, N. J., Kanekal, S., Kessel, R., Sibeck, D., & Ukhorskiy, a. A. (2013). *Science objectives and rationale for the radiation belt storm probes mission* (pp. 3–27). The van Allen probes mission.

McPherson, D. A., & Koons, H. C. (1970). Dependence of elf emissions on the location of the plasmapause. *Journal of Geophysical Research (1896-1977)*, *75*(28), 5559–5564. https://doi.org/10.1029/JA075i028p05559

Meredith, N. P., Horne, R. B., & Anderson, R. R. (2001). Substorm dependence of chorus amplitudes: Implications for the acceleration of electrons to relativistic energies. *Journal of Geophysical Research*, *106*(A7), 13165–13178. https://doi.org/10.1029/2000JA900156

Meredith, N. P., Horne, R. B., Shen, X., Li, W., & Bortnik, J. (2020). *Global model of whistler mode chorus in the near-equatorial region*. Geophysical Research Letters. https://doi.org/10.1029/2020GL087311

Meredith, N. P., Horne, R. B., Sicard-Piet, A., Boscher, D., Yearby, K. H., Li, W., & Thorne, R. M. (2012). Global model of lower band and upper band chorus from multiple satellite observations. *Journal of Geophysical Research*, *117*(A10). https://doi.org/10.1029/2012JA017978

Meredith, N. P., Horne, R. B., Summers, D., Thorne, R. M., Iles, R. H. A., Heynderickx, D., & Anderson, R. R. (2002). Evidence for acceleration of outer zone electrons to relativistic energies by whistler mode chorus. *Annals of Geophysics*, *20*(7), 967–979. https://doi.org/10.5194/angeo-20-967-2002

Meredith, N. P., Horne, R. B., Thorne, R. M., & Anderson, R. R. (2009). Survey of upper band chorus and ECH waves: Implications for the diffuse aurora. *Journal of Geophysical Research*, *114*(A7). https://doi.org/10.1029/2009JA014230

Meredith, N. P., Horne, R. B., Thorne, R. M., Summers, D., & Anderson, R. R. (2004). Substorm dependence of plasmaspheric hiss. *Journal of Geophysical Research*, *109*(A6). https://doi.org/10.1029/2004JA010387

Moldwin, M. B., Downward, L., Rassoul, H. K., Amin, R., & Anderson, R. R. (2002). A new model of the location of the plasmapause: CRRES results. *Journal of Geophysical Research*, *107*(A11), SMP2-1–9. https://doi.org/10.1029/2001JA009211

Mourenas, D., Zhang, X.-J., Artemyev, A. V., Angelopoulos, V., Thorne, R. M., Bortnik, J., et al. (2018). Electron nonlinear resonant interaction with short and intense parallel chorus wave packets. *Journal of Geophysical Research: Space Physics*, *123*(6), 4979–4999. https://doi.org/10.1029/2018JA025417

Němec, F., Santolík, O., Hospodarsky, G. B., Kurth, W. S., & Kletzing, C. (2022). Power line harmonic radiation observed by the Van Allen Probes spacecraft. *Journal of Geophysical Research: Space Physics*, *127*(6), e2022JA030320. https://doi.org/10.1029/2022JA030320

Ni, B., Thorne, R. M., Shprits, Y. Y., & Bortnik, J. (2008). Resonant scattering of plasma sheet electrons by whistler-mode chorus: Contribution to diffuse auroral precipitation. *Geophysical Research Letters*, *35*(11). https://doi.org/10.1029/2008GL034032

Paschmann, G., & Schwartz, S. (2000). ISSI book on analysis methods for multi-spacecraft data (Vol. *449*).

Reeves, G. D., Chen, Y., Cunningham, G. S., Friedel, R. W. H., Henderson, M. G., Jordanova, V. K., et al. (2012). Dynamic radiation environment assimilation model: Dream. *Space Weather*, *10*(3). https://doi.org/10.1029/2011SW000729

Ripoll, J.-F., Thaller, S. A., Hartley, D. P., Cunningham, G. S., Pierrard, V., Kurth, W. S., et al. (2022). Statistics and empirical models of the plasmasphere boundaries from the Van Allen Probes for radiation belt physics. *Geophysical Research Letters*, *49*(21), e2022GL101402. https://doi.org/10.1029/2022GL101402

Ross, J. P. J., Glauert, S. A., Horne, R. B., Watt, C. E. J., & Meredith, N. P. (2021). On the variability of emic waves and the consequences for the relativistic electron radiation belt population. *Journal of Geophysical Research: Space Physics*, *126*(12), e2021JA029754. https://doi.org/10.1029/2021JA029754

Ross, J. P. J., Glauert, S. A., Horne, R. B., Watt, C. E., Meredith, N. P., & Woodfield, E. E. (2020). A new approach to constructing models of electron diffusion by emic waves in the radiation belts. *Geophysical Research Letters*, *47*(20), e2020GL088976. https://doi.org/10.1029/2020GL088976

Santolík, O., Gurnett, D. A., Pickett, J. S., Parrot, M., & Cornilleau-Wehrlin, N. (2003). Spatio-temporal structure of storm-time chorus. *Journal of Geophysical Research*, *108*(A7). https://doi.org/10.1029/2002JA009791

Santolík, O., Kletzing, C. A., Kurth, W. S., Hospodarsky, G. B., & Bounds, S. R. (2014). Fine structure of large-amplitude chorus wave packets. *Geophysical Research Letters*, *41*(2), 293–299. https://doi.org/10.1002/2013GL058889

Santolík, O., Parrot, M., & Lefeuvre, F. (2003). Singular value decomposition methods for wave propagation analysis. *Radio Science*, *38*(1). https://doi.org/10.1029/2000RS002523

Seo, J., & Kim, K.-C. (2023). The relationship of exohiss waves with plasmaspheric hiss distribution and solar wind parameters. *Journal of Geophysical Research: Space Physics*, *128*(10), e2023JA031777. https://doi.org/10.1029/2023JA031777

Shane, A. D., Marshall, R. A., Wold, A. M., Shen, X.-C., & Li, W. (2025). Lightning generated whistlers: Variability of event-based wave distributions. *Journal of Geophysical Research: Space Physics*, *130*(8), e2025JA034164. https://doi.org/10.1029/2025JA034164

Sheeley, B. W., Moldwin, M. B., Rassoul, H. K., & Anderson, R. R. (2001). An empirical plasmasphere and trough density model: CRRES observations. *Journal of Geophysical Research*, *106*(A11), 25631–25641. https://doi.org/10.1029/2000JA000286

Shprits, Y. Y., Subbotin, D. A., Meredith, N. P., & Elkington, S. R. (2008). Review of modeling of losses and sources of relativistic electrons in the outer radiation belt II: Local acceleration and loss. *Journal of Atmospheric and Solar-Terrestrial Physics*, *70*(14), 1694–1713. https://doi.org/10.1016/j.jastp.2008.06.014

Shue, J.-H., Nariyuki, Y., Katoh, Y., Saito, S., Kasahara, Y., Hsieh, Y.-K., et al. (2019). A systematic study in characteristics of lower band rising-tone chorus elements. *Journal of Geophysical Research: Space Physics*, *124*(11), 9003–9016. https://doi.org/10.1029/2019JA027368

Stix, T. (1992). *Waves in plasmas*. American Inst. of Physics. Retrieved from https://books.google.co.uk/books?id=OsOWJ8iHpmMC

Su, Z., Liu, N., Zheng, H., Wang, Y., & Wang, S. (2018). Multipoint observations of nightside plasmaspheric hiss generated by substorm-injected electrons. *Geophysical Research Letters*, *45*(20), 10921–10932. https://doi.org/10.1029/2018GL079927

Subbotin, D., Shprits, Y., & Ni, B. (2010). Three-dimensional verb radiation belt simulations including mixed diffusion. *Journal of Geophysical Research*, *115*(A3). https://doi.org/10.1029/2009JA015070

Summers, D., Thorne, R. M., & Xiao, F. (1998). Relativistic theory of wave-particle resonant diffusion with application to electron acceleration in the magnetosphere. *Journal of Geophysical Research*, *103*(A9), 20487–20500. https://doi.org/10.1029/98JA01740

Tao, X., An, Z., Zonca, F., Chen, L., & Bortnik, J. (2025). Chorus wave–driven electron dynamics in the Van Allen belts: From coherence to diffusion. *AGU Advances*, *6*(6), e2025AV001990. https://doi.org/10.1029/2025AV001990

Tao, X., Li, W., Bortnik, J., Thorne, R. M., & Angelopoulos, V. (2012). Comparison between theory and observation of the frequency sweep rates of equatorial rising tone chorus. *Geophysical Research Letters*, *39*(8). https://doi.org/10.1029/2012GL051413

Teng, S., Tao, X., & Li, W. (2019). Typical characteristics of whistler mode waves categorized by their spectral properties using Van Allen Probes observations. *Geophysical Research Letters*, *46*(7), 3607–3614. https://doi.org/10.1029/2019GL082161

Thaller, S. A., Wygant, J. R., Dai, L., Breneman, A. W., Kersten, K., Cattell, C. A., et al. (2015). Van Allen Probes investigation of the large-scale duskward electric field and its role in ring current formation and plasmasphere erosion in the 1 June 2013 storm. *Journal of Geophysical Research: Space Physics*, *120*(6), 4531–4543. https://doi.org/10.1002/2014JA020875

Thorne, R. M., Smith, E. J., Burton, R. K., & Holzer, R. E. (1973). Plasmaspheric HISS. *Journal of Geophysical Research (1896-1977)*, *78*(10), 1581–1596. https://doi.org/10.1029/JA078i010p01581

Tong, Y., Vasko, I. Y., Artemyev, A. V., Bale, S. D., & Mozer, F. S. (2019). Statistical Study of Whistler Waves in the Solar Wind at 1 au. *The Astrophysical Journal*, *878*(1), 41. https://doi.org/10.3847/1538-4357/ab1f05

Tsurutani, B. T., & Smith, E. J. (1974). Postmidnight chorus: A substorm phenomenon. *Journal of Geophysical Research (1896-1977)*, *79*(1), 118–127. https://doi.org/10.1029/JA079i001p00118

Tyler, E., Breneman, A., Cattell, C., Wygant, J., Thaller, S., & Malaspina, D. (2019a). Statistical distribution of whistler mode waves in the radiation belts with large magnetic field amplitudes and comparison to large electric field amplitudes. *Journal of Geophysical Research: Space Physics*, *124*(8), 6541–6552. https://doi.org/10.1029/2019JA026913

Tyler, E., Breneman, A., Cattell, C., Wygant, J., Thaller, S., & Malaspina, D. (2019b). Statistical occurrence and distribution of high-amplitude whistler mode waves in the outer radiation belt. *Geophysical Research Letters*, *46*(5), 2328–2336. https://doi.org/10.1029/2019GL082292

Varotsou, A., Boscher, D., Bourdarie, S., Horne, R. B., Glauert, S. A., & Meredith, N. P. (2005). Simulation of the outer radiation belt electrons near geosynchronous orbit including both radial diffusion and resonant interaction with whistler-mode chorus waves. *Geophysical Research Letters*, *32*(19). https://doi.org/10.1029/2005GL023282

Varotsou, A., Boscher, D., Bourdarie, S., Horne, R. B., Meredith, N. P., Glauert, S. A., & Friedel, R. H. (2008). Three-dimensional test simulations of the outer radiation belt electron dynamics including electron-chorus resonant interactions. *Journal of Geophysical Research*, *113*(A12). https://doi.org/10.1029/2007JA012862

Wang, D., Shprits, Y. Y., Zhelavskaya, I. S., Agapitov, O. V., Drozdov, A. Y., & Aseev, N. A. (2019). Analytical chorus wave model derived from Van Allen Probe observations. *Journal of Geophysical Research: Space Physics*, *124*(2), 1063–1084. https://doi.org/10.1029/2018JA026183

Wang, J. L., Li, L. Y., & Yu, J. (2020). Statistical relationship between exohiss waves and plasmaspheric hiss. *Geophysical Research Letters*, *47*(5), e2020GL087023. https://doi.org/10.1029/2020GL087023

Watt, C. E. J., Allison, H. J., Meredith, N. P., Thompson, R. L., Bentley, S. N., Rae, I. J., et al. (2019). Variability of quasilinear diffusion coefficients for plasmaspheric HISS. *Journal of Geophysical Research: Space Physics*, *124*(11), 8488–8506. https://doi.org/10.1029/2018JA026401

Watt, C. E. J., Meredith, N. P., Wong, J., Murphy, K. R., Rae, I. J., Chakraborty, S., et al. (2025). Occurrence rates and variability of whistler-mode waves in the plasma trough. *Journal of Geophysical Research: Space Physics*, *130*(10), e2025JA034061. https://doi.org/10.1029/2025JA034061

Watt, C. E. J., Rae, I. J., Murphy, K. R., Anekallu, C., Bentley, S. N., & Forsyth, C. (2017). The parameterization of wave-particle interactions in the outer radiation belt. *Journal of Geophysical Research: Space Physics*, *122*(9), 9545–9551. https://doi.org/10.1002/2017JA024339

Wong, J.-M., Meredith, N. P., Horne, R. B., Glauert, S. A., & Ross, J. P. J. (2024). New chorus diffusion coefficients for radiation belt modeling. *Journal of Geophysical Research: Space Physics*, *129*(1), e2023JA031607. https://doi.org/10.1029/2023JA031607

Wygant, J., Bonnell, J., Goetz, K., Ergun, R., Mozer, F., & Bale, S. (2013). *The electric field and waves instruments on the radiation belt storm probes mission* (pp. 183–220). The Van Allen Probes Mission.

Zhang, S., Rae, I. J., Watt, C. E. J., Degeling, A. W., Tian, A., Shi, Q., et al. (2021). Determining the temporal and spatial coherence of plasmaspheric hiss waves in the magnetosphere. *Journal of Geophysical Research: Space Physics*, *126*(2), e2020JA028635. https://doi.org/10.1029/2020JA028635

Zhang, X.-J., Agapitov, O., Artemyev, A. V., Mourenas, D., Angelopoulos, V., Kurth, W. S., et al. (2020). Phase decoherence within intense chorus wave packets constrains the efficiency of nonlinear resonant electron acceleration. *Geophysical Research Letters*, *47*(20), e2020GL089807. https://doi.org/10.1029/2020GL089807

Zhang, X.-J., Mourenas, D., Artemyev, A. V., Angelopoulos, V., Bortnik, J., Thorne, R. M., et al. (2019). Nonlinear electron interaction with intense chorus waves: Statistics of occurrence rates. *Geophysical Research Letters*, *46*(13), 7182–7190. https://doi.org/10.1029/2019GL083833

Zhang, X.-J., Thorne, R., Artemyev, A., Mourenas, D., Angelopoulos, V., Bortnik, J., et al. (2018). Properties of intense field-aligned lower-band chorus waves: Implications for nonlinear wave-particle interactions. *Journal of Geophysical Research: Space Physics*, *123*(7), 5379–5393. https://doi.org/10.1029/2018JA025390

Zhou, Q., Li, J., Xiao, F., Zhang, S., Liu, S., Yang, C., et al. (2023). Global occurrence of higher-bands ECH waves in radiation belts based on a novel noise reduction algorithm (NORA). *Geophysical Research Letters*, *50*(6), e2022GL101889. https://doi.org/10.1029/2022GL101889

Zhu, H., Gu, W., & Chen, L. (2019). Statistical analysis on plasmatrough exohiss waves from the Van Allen Probes. *Journal of Geophysical Research: Space Physics*, *124*(6), 4356–4364. https://doi.org/10.1029/2018JA026359

Zou, W., Li, H., Hu, P., Wang, D., Tang, R., Ouyang, Z., et al. (2024). Statistical properties of exohiss waves and associated scattering losses of radiation belt electrons. *Journal of Geophysical Research: Space Physics*, *129*(5), e2023JA032244. https://doi.org/10.1029/2023JA032244